JCB Journal of Cell Biology

ARTICLE

Par-1 controls the composition and growth of cortical actin caps during *Drosophila* embryo cleavage

Tao Jiang and Tony J.C. Harris

Cell structure depends on the cortex, a thin network of actin polymers and additional proteins underlying the plasma membrane. The cell polarity kinase Par-1 is required for cells to form following syncytial *Drosophila* embryo development. This requirement stems from Par-1 promoting cortical actin caps that grow into dome-like metaphase compartments for dividing syncytial nuclei. We find the actin caps to be a composite material of Diaphanous (Dia)-based actin bundles interspersed with independently formed, Arp2/3-based actin puncta. Par-1 and Dia colocalize along extended regions of the bundles, and both are required for the bundles and for each other's bundle-like localization, consistent with an actin-dependent self-reinforcement mechanism. Par-1 helps establish or maintain these bundles in a cortical domain with relatively low levels of the canonical formin activator Rho1-GTP. Arp2/3 is required for displacing the bundles away from each other and toward the cap circumference, suggesting interactions between these cytoskeletal components could contribute to the growth of the cap into a metaphase compartment.

Introduction

A variety of proteins are recruited to the inner surface of the plasma membrane to form the cell cortex. Moreover, specialized cortical domains contribute to a wide range of cellular processes, including division, migration, and adhesion. However, we lack a full understanding of the relationships among cortical proteins, or how these interactions affect the cell.

F-actin networks form a major part of the cell cortex. Actin-binding proteins link F-actin to the plasma membrane by binding lipid head groups or integral membrane proteins (Chugh and Paluch, 2018). F-actin can grow as Arp2/3-induced branched networks and as extended formin-induced filaments that can be drawn into bundles. The growth of either network can create specific cortical domains for extending cell protrusions, cell–cell contacts, and other structures. Reciprocally, engagement with nonmuscle myosin II (referred to as myosin hereafter) forms actomyosin networks for constricting cortical domains (Lecuit et al., 2011; Skau and Waterman, 2015). Rho family small G proteins activate these players (Lawson and Ridley, 2018; Zuo et al., 2014). For example, RhoA-GTP can activate formins by relief of auto-inhibition, although additional factors contribute to formin-based actin assembly in vivo (Kühn and Geyer, 2014).

The cell cortex also contains cell polarity proteins (Goldstein and Macara, 2007; Lang and Munro, 2017; St Johnston and Ahringer, 2010; Tepass, 2012). For example, Par proteins can interact with the plasma membrane through binding to lipids or integral membrane proteins. One role of the Par proteins is to polarize the cell cortex into two major domains for apico-basal epithelial cell polarity or asymmetric cell division. This polarization occurs through kinases of one domain inhibiting the membrane association of proteins of the opposite domain. For example, the apical kinase aPKC phosphorylates and inhibits the cortical association of the basolateral kinase Par-1. The system is reinforced by mutual antagonism between the two domains, as exemplified by Par-1 phosphorylating and inhibiting the cortical association of the aPKC-interacting protein Par-3/Bazooka (Baz). Although mechanisms of Par protein polarization are well-defined, it is less clear how Par proteins affect other cortical components for control of cell structure and behavior.

Like its vertebrate homologues, *Drosophila melanogaster* Par-1 is a multi-domain protein that functions in a range of cell types and processes (McDonald, 2014; Wu and Griffin, 2017). A cortical association domain is regulated by aPKC phosphorylation (Doerflinger et al., 2010; Vaccari et al., 2005). Its kinase domain

Department of Cell and Systems Biology, University of Toronto, Toronto, Ontario, Canada.

Correspondence to Tony J.C. Harris: tony.harris@utoronto.ca.

phosphorylates Par-3/Baz and several other proteins for the polarization of a number of cell types (Benton and St Johnston, 2003; Riechmann and Ephrussi, 2004; Riechmann et al., 2002; Zhang et al., 2007). Moreover, Par-1 phosphorylates a myosin phosphatase subunit (myosin binding subunit; Mbs; Majumder et al., 2012) and the microtubule interacting protein Tau (Nishimura et al., 2004). In the *Drosophila* embryo ectoderm, Par-1 promotes apico-basal polarity (Bayraktar et al., 2006; Jiang et al., 2015; McKinley and Harris, 2012), but in the early syncytial embryo, Par-1 has functions apparently distinct from this polarization. Before aPKC-induced displacement from the apical domain at the end of cellularization (Jiang et al., 2015), Par-1 is nonpolarized, localizing over the full cell cortex (McKinley and Harris, 2012). At this early stage, Par-1 is required for cellularization furrows (McKinley and Harris, 2012), but the mechanism involved is unknown.

The syncytial *Drosophila* embryo undergoes multiple rounds of synchronous nuclear division without cell division (Foe and Alberts, 1983). At nuclear cycle 10, most nuclei translocate to the periphery of the single-cell embryo and individually induce local dome-shaped compartments from the initially flat cortex (Fig. 1 A). These compartments anchor and separate mitotic spindles of the dividing nuclei. The ingressed plasma membranes between neighboring compartments are termed "pseudo-cleavage" or "metaphase" furrows; we will describe a single compartment as a "metaphase compartment." They form and regress for each division cycle until cycle 14, when cellularization furrows ingress deeply into the embryo and close off beneath each nucleus. Each nucleus induces its metaphase compartment through signals from its associated centrosomes (Raff and Glover, 1989; Stevenson et al., 2001). These signals trigger polymerization of a cortical actin cap above each nucleus, and, simultaneously, actomyosin networks assemble in a distinct cortical domain encircling each cap (Foe et al., 2000). Rac small G protein signaling induces Arp2/3 networks of the actin caps (Postner et al., 1992; Stevenson et al., 2002; Zallen et al., 2002; Zhang et al., 2018). Rho1 signaling induces myosin assembly in the borders (Crest et al., 2012; Royou et al., 2004) and is also required for cap growth (Cao et al., 2010), roles similar to the formin Diaphanous (Dia), which affects both the actomyosin borders and the actin caps (Afshar et al., 2000; Cao et al., 2010). The actin caps and actomyosin borders expand and meet as distinct cortical domains. Each actin cap continues its centrifugal growth but then bends inward through buckling and swelling to form a dome-shaped compartment with a narrowed actomyosin network lining its basal rim (Zhang et al., 2018). Remarkably, metaphase compartments can form independently of myosin activity (Royou et al., 2004), with growth of the actin cap against residual components of its border sufficing for cortical buckling (Zhang et al., 2018). Although the actin cap is the major inducer of the metaphase compartment (Postner et al., 1992; Stevenson et al., 2002; Zallen et al., 2002; Zhang et al., 2018), how Arp2/3 and Dia function together to power cap growth is unclear. Also, although RhoGEF2 promotes full Dia recruitment to actomyosin networks at the base of cellularization furrows (Grosshans et al., 2005), and Dia binds and recruits APC2 for metaphase furrow formation (Webb et al., 2009), how Dia-based actin polymerization occurs in growing caps is not understood.

Here, we show that Par-1 is required for actin cap growth and metaphase compartment formation. More specifically, Par-1 is needed for Dia-based actin bundles in the cap, a cortical domain with relatively low Rho1-GTP. Dia and Par-1 display striking colocalization along extended regions of the bundles, and both are required for the bundles and for each other's bundle-like localization, suggesting a self-reinforcement mechanism. Significantly, the bundles form with independence from cap Arp2/3 networks, and vice versa. The Arp2/3 networks appear to push against the bundles for growth of the cap into a metaphase compartment. Our data reveal a functional interaction between Dia and Par-1 important for actin bundles that engage Arp2/3 networks within a composite cortical material that shapes the cell.

Results

Metaphase compartments require Par-1 kinase activity but not known phosphorylation targets

To assess the role of Par-1 during syncytial cleavage of the *Drosophila* embryo, we expressed *par-1* shRNA maternally and stained embryos for F-actin and tubulin to detect the cell cortex and cell cycle stage, respectively. At metaphase, phalloidin-stained furrows were often broken or fully lost in *par-1* RNAi embryos versus controls (Fig. 1, B and C). In contrast, spindles were individually similar in control and *par-1* RNAi embryos, but abnormal contacts between spindles occurred where furrows were disrupted by *par-1* RNAi (Fig. 1 B, yellow arrowheads; similar results observed with two independent microtubule markers imaged live; Fig. S1, A–C). Interphase microtubules seemed unaffected by *par-1* RNAi (Fig. S1 D). To test the specificity of the *par-1* RNAi effect, we coexpressed an RNAi-resistant and GFP-tagged form of Par-1 and found that it reversed the furrow defects (Fig. 1, B and C). In contrast, an otherwise equivalent Par-1 construct with two mutations that compromise its kinase activity (Vaccari et al., 2005) failed to rescue the *par-1* RNAi defects, even though it localized to compartment furrows to a similar extent as the active construct (Fig. 1, B and C). Thus, Par-1 kinase activity promotes metaphase compartment formation in syncytial *Drosophila* embryos without apparent effects on individual microtubule networks.

In addition to considering microtubules, we evaluated other reported Par-1 effectors, focusing on three proteins known to be inhibited by Par-1 phosphorylation. First, we tested Par-1 phosphorylation of Mbs by expressing a nonphosphorylatable form of Mbs known to be hyperactive (Majumder et al., 2012). As expected for increased myosin phosphatase activity, the construct depleted cortical myosin, but left metaphase compartments intact (Fig. S2 A) except for extended bands of compartment disorganization (Fig. S2 A, brackets). Such abnormal bands result from defective axial expansion of syncytial nuclei before their migration to the cortex (Royou et al., 2002) and are distinct from the effects of *par-1* RNAi. Next, we

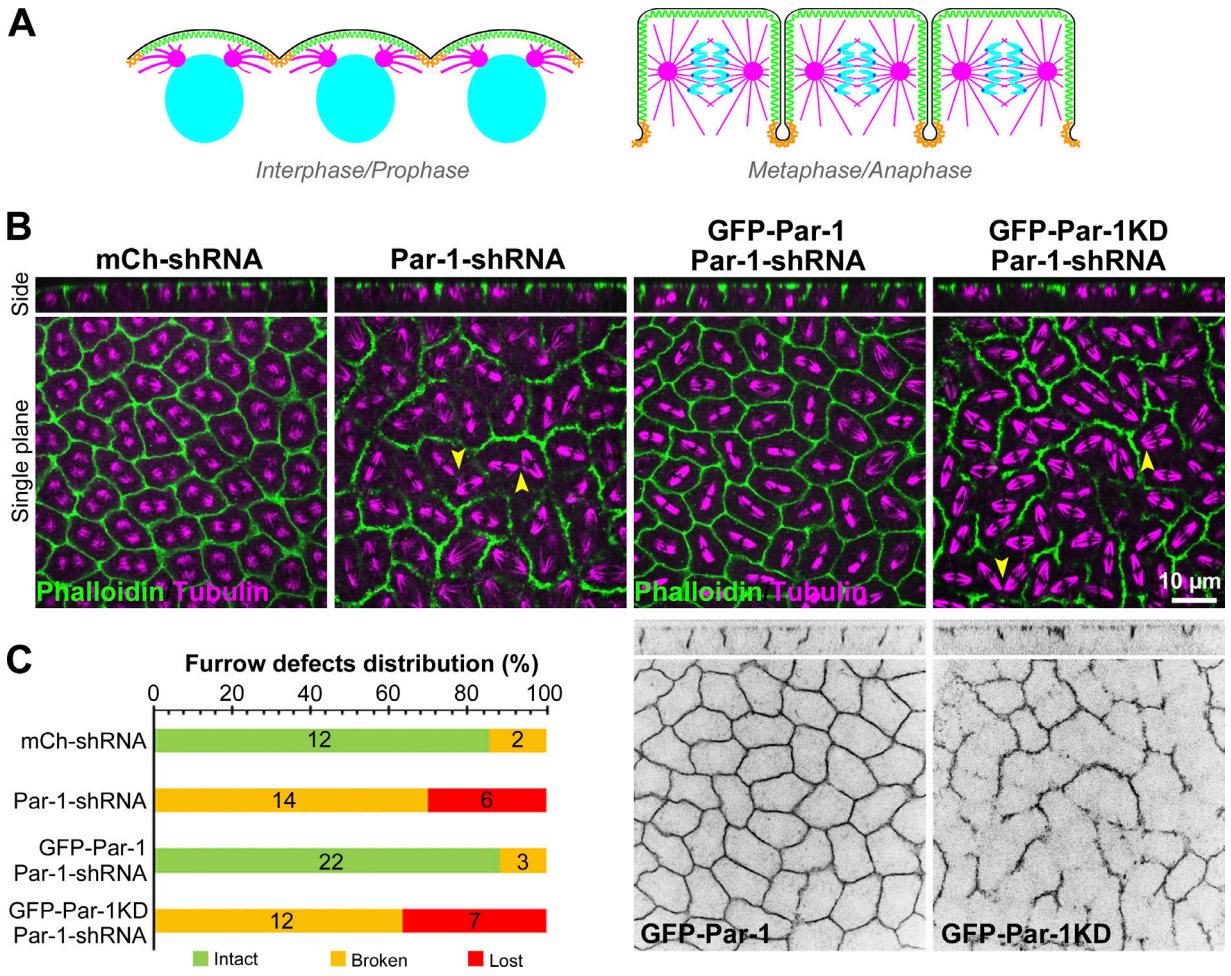

Figure 1. **Par-1 kinase activity is required for *Drosophila* embryo metaphase compartments. (A)** Schematic side views of three cortical nuclei. At interphase and prophase, each nucleus induces an apical actin cap (green) encircled by an actomyosin border (orange; shown in cross section). By metaphase, each cap grows into a compartment for a mitotic spindle. **(B)** Cycle 12 metaphase. For control RNAi embryos (shRNA targeting nonexpressed mCherry), phalloidin-stained (F-actin positive) furrows fully surround each tubulin-stained mitotic spindle. With *par-1* RNAi, many furrows are lost, and abnormal interspindle contacts arise (arrowheads). Coexpression of RNAi-resistant GFP–Par-1 rescues the *par-1* RNAi defects, but a kinase-deficient (KD) version does not. Both Par-1 constructs localize to the embryo cortex (bottom right panels). **(C)** Furrow defects quantified as three classes (see Materials and methods). Embryo numbers on the bars.

examined two scaffold proteins that affect cortical polarity and are phosphorylated by Par-1. We evaluated Par-1 phosphorylation of Baz by overexpressing a nonphosphorylatable form of Baz known to mislocalize in polarized epithelial cells (Benton and St Johnston, 2003; McKinley and Harris, 2012), but no compartment defects were induced (Fig. S2 B). We also examined Dlg, which is displaced from neuro-muscular junctions by Par-1 phosphorylation (Zhang et al., 2007). However, substantially reducing Dlg cortical levels by coexpressing *dlg* and *par-1* shRNAs failed to reverse the *par-1* shRNA defects (Fig. S2 C). *dlg* RNAi alone did not result in compartment furrow loss (Fig. S2 C). Thus, misregulation of Mbs, Baz, or Dlg has no detectable role in the failed compartmentalization of Par-1–depleted embryos.

Par-1 localizes to actin caps, actomyosin borders, and microtubule networks

To investigate how Par-1 promotes metaphase compartments, we examined the subcellular localization of the RNAi-resistant, kinase-active GFP–Par-1 construct acting in place of RNAi-depleted endogenous Par-1. At interphase (Fig. 2 A, time 0), the GFP–Par-1 construct was enriched in both actin caps (Fig. 2 A, brackets) and actomyosin borders (Fig. 2 A, yellow arrows), and also decorated centrosomes (Fig. 2 A, purple arrows). Within the caps, GFP–Par-1–labeled punctate and bundle-like structures (Fig. 2 A, time 0; white arrows indicate bundles). From prophase to anaphase, apical surface levels of Par-1 diminished, while levels were maintained along the furrows and in the actomyosin zone at their basal tips, as well as to elements of microtubule networks (Fig. 2 A; 2 min, 37 s to 10 min, 30 s). Imaging of Par-1–GFP expressed from a homozygous viable GFP-trap *par-1* allele revealed similar localization patterns as the RNAi-resistant GFP–Par-1 construct (Fig. 2 B), but the signal was weaker. These data show localization of Par-1 to the two main cortical domains of the metaphase compartments: the actin caps and actomyosin borders.

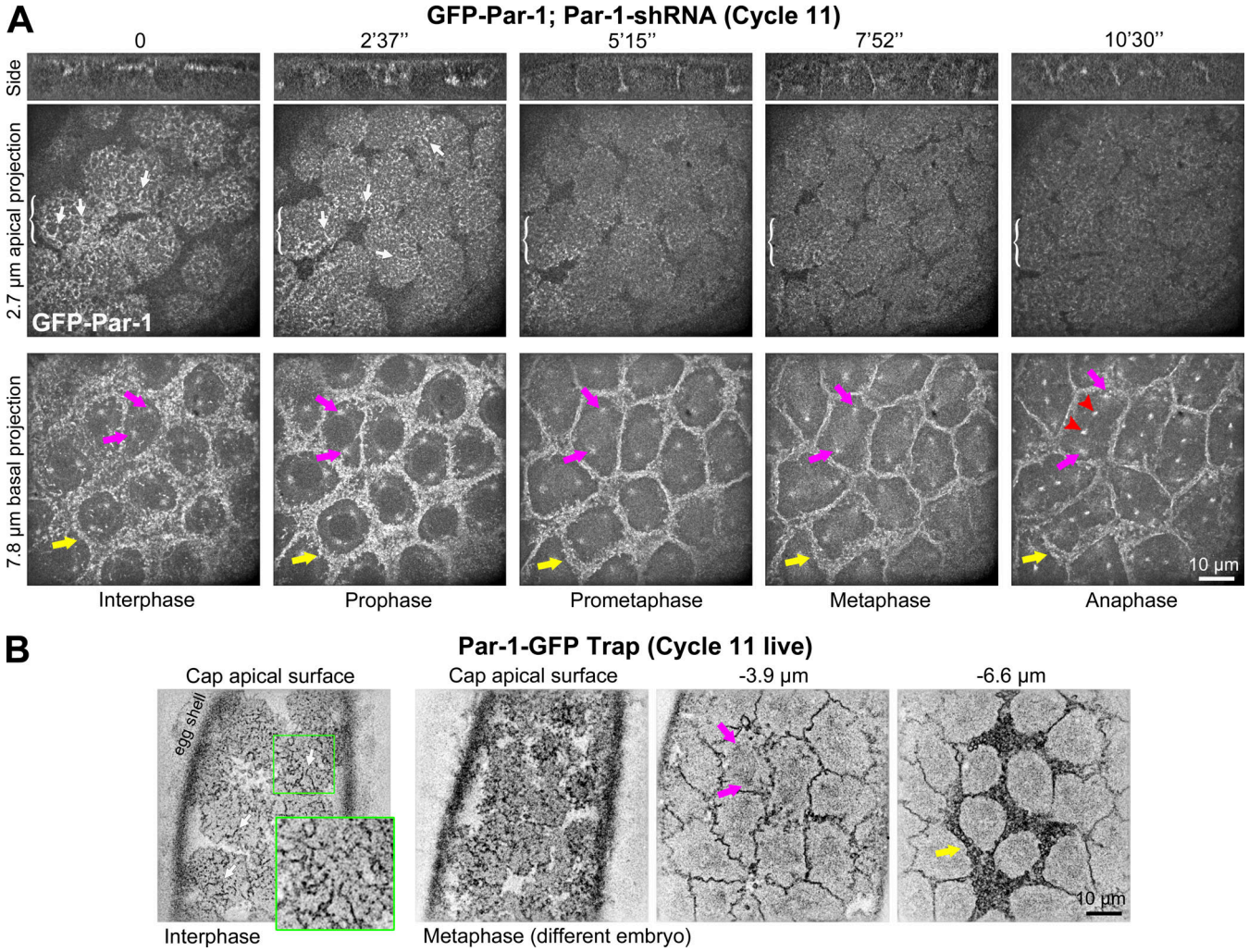

Figure 2. **Par-1 localizes to actin cap bundles, actomyosin borders, and mitotic spindles. (A)** Overexpressed GFP–Par-1 live with RNAi depletion of endogenous Par-1. Apical projections show caps (one bracketed). At interphase and prophase, GFP–Par-1 localizes to cap bundles (white arrows), a pattern that dissipates into metaphase and anaphase. Basal projections show GFP–Par-1 at the actomyosin border of each cap (yellow arrows), at centrosomes (purple arrows), and at portions of the anaphase central spindle (red arrowheads). Time = 0 is arbitrary. **(B)** Par-1–GFP expressed from an endogenous gene trap. At interphase, Par-1–GFP in cap bundles (white arrows and inset). At metaphase, Par-1–GFP enriched at actin cap accumulations, mitotic spindle centrosomes (purple arrows), and actomyosin borders (yellow arrow). Photobleaching of weakly expressed Par-1–GFP hindered full cell cycle imaging of the same embryo. **(A and B)** Images deconvolved. Time given in minutes and seconds.

Par-1 promotes actin cap growth for metaphase compartment formation

We next examined *par-1* RNAi embryos expressing a probe that decorates F-actin: Moesin actin-binding domain (Moe-ABD)–GFP (Kiehart et al., 2000). Starting with early cortical divisions, control actin cap networks grew centrifugally (Fig. 3 A, yellow brackets), gained contact with neighboring caps, and ingressed to form metaphase furrows (Fig. 3 A, green arrows). At the same nuclear division cycles, *par-1* RNAi actin cap networks initiated, but grew slower than controls (Fig. 3 A, yellow brackets; quantified in Fig. 3 B), and formed fewer furrows (Fig. 3 A, green arrows; quantified in Fig. S3 A). This cap growth defect resembled that revealed by Moe-ABD–GFP imaging in *dia* RNAi embryos (Fig. 3 A) and *Arp3* RNAi embryos (Zhang et al., 2018).

To assess actomyosin borders, we imaged Zipper (Zip)-GFP (nonmuscle myosin heavy chain) expressed from a homozygous viable GFP-trap allele. During early cortical divisions in control RNAi embryos, Zip-GFP first accumulated to broad domains around each cap, and these borders then thinned and ingressed at the basal tips of metaphase furrows (Zhang et al., 2018; Fig. S3 B). During early cortical divisions of *par-1* RNAi embryos, the Zip-GFP–positive borders were initially somewhat broader than controls (Fig. S3 B; an effect accentuated with fixation; see Fig. 8), and then thinned with subtle fragmentation (Fig. S3 B). The myosin-positive furrow tips ingressed less deeply than controls (Fig. S3 C). Similar subtle effects on the Zip-GFP networks were apparent during early cortical divisions with *dia* RNAi (Fig. S3, B and C). For both *par-1* RNAi and *dia* RNAi embryos, stronger fragmentation of the actomyosin borders occurred at later nuclear division

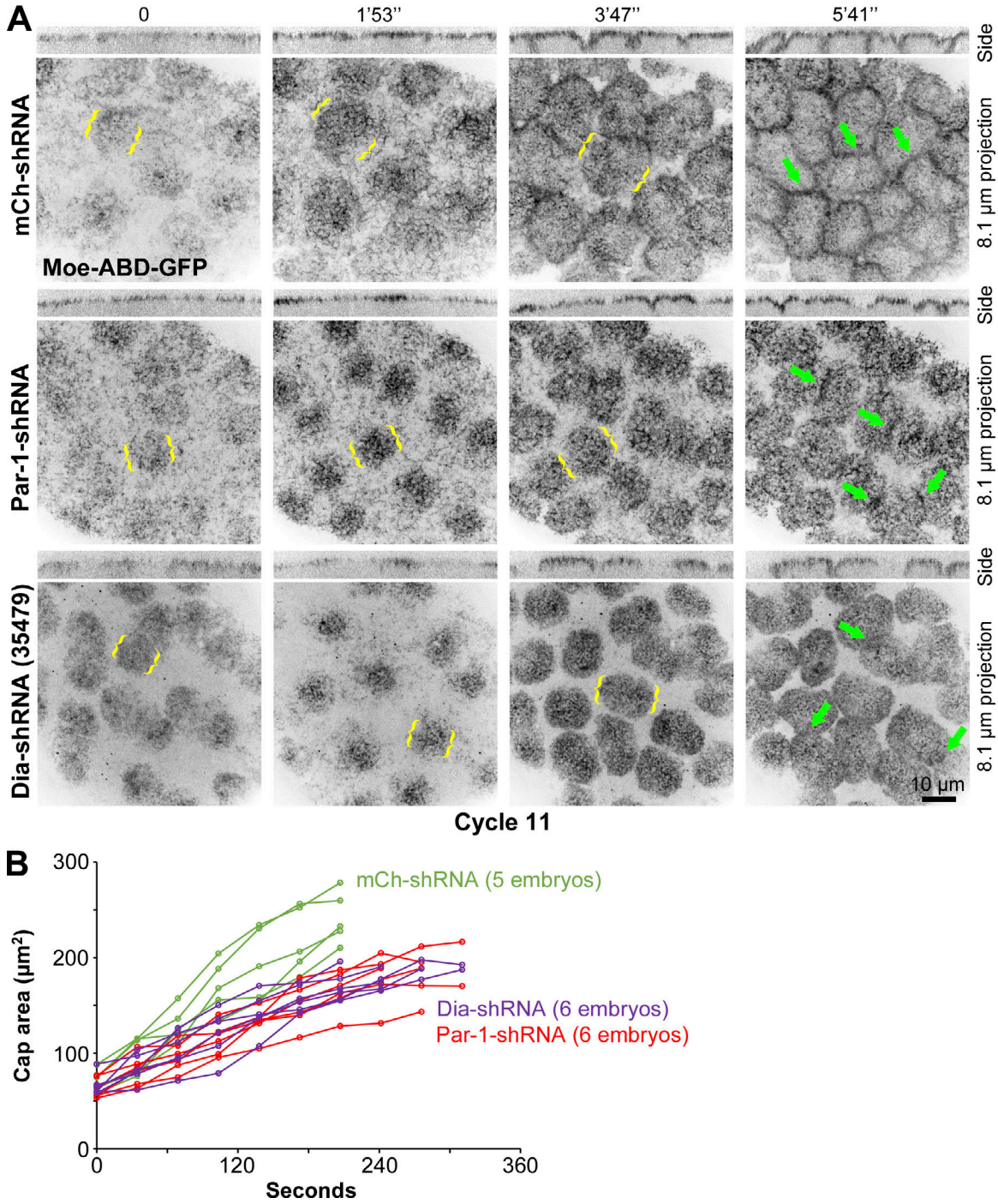

Figure 3. **Depletion of Par-1 or Dia reduces cap growth. (A)** Moe-ABD–GFP decorates the caps. For control mCherry RNAi, each cap grows centrifugally in the apical plane (one cap bracketed) and then bends inward, forming compartment furrows (green arrows). With *par-1* or *dia* RNAi, caps initiate, but centrifugal growth (one cap bracketed) and furrows (green arrows) are reduced. Time = 0 is arbitrary. Genotypes begin at the same stage. **(B)** Cap area versus time for control, *par-1*, and *dia* RNAi cycle 11 embryos. Caps quantified every third time frame from initial appearance to their meeting with neighboring caps (see Materials and methods). Just before the meeting of neighboring control caps (207 s), cap areas were significantly larger for controls versus *par-1* or *dia* RNAi ($P < 0.01$ for each comparison). Time given in minutes and seconds.

cycles and persisted into cellularization (Videos 1, 2, and 3). Notably, these stronger Zip-GFP abnormalities arose at later cycles than the cap growth defects (compare with Fig. 3 A). Also, distinct effects on the Zip-GFP distributions were apparent. *par-1* RNAi embryos retained long bands of myosin that ran between multiple compartments, whereas *dia* RNAi embryos underwent fragmentation of myosin into small patches (Videos 1, 2, and 3). In contrast to both cases, the actomyosin borders of *Arp3* RNAi embryos remain abnormally broad without fragmentation (Zhang et al., 2018).

Par-1 and Dia have similar effects on cap actin structure that are distinct from those of Arp3

Since cap growth is promoted by Par-1, Dia, and Arp3, we examined cap actin organization in greater detail and compared the effects of each protein. Embryo fixation and phalloidin staining revealed two organizations of F-actin within a normally forming cap: extended bundles and numerous, smaller puncta (Fig. 4 A, arrows indicates bundles). At metaphase, fixed and phalloidin-stained bundles existed over the apical cap surface and ran into stronger F-actin bands that coated ingressed furrows (Fig. 4 A). In contrast, *par-1* RNAi embryos displayed only small puncta throughout both forming and metaphase caps, a granular appearance shared by *dia* RNAi embryos at both stages (Fig. 4 A). Strikingly, *Arp3* RNAi caps were dominated by actin bundles at each stage (Fig. 4 A, arrows). These data show that the effect of Par-1 on cap actin is similar to that of Dia and distinct from that of Arp3 (quantified in Fig. 4 C). Moreover, it appears that caps are composed of two distinguishable actin networks in wild-type embryos and that granular Arp2/3 networks mainly form with *par-1* or *dia* RNAi, whereas Dia-based actin bundles mainly form with *Arp3* RNAi. Indeed, the *Arp3* RNAi caps were enriched for both Dia and GFP–Par-1 (Fig. 4 B).

Par-1 and Dia interact genetically

To further test whether Par-1 promotes Dia-based actin bundles for cap growth and metaphase compartmentalization, we examined the effects of a weaker *dia* shRNA construct with additional depletion or elevation of Par-1 activity (differing *dia* shRNA strengths were apparent from cellularization analyses). To reduce Par-1 activity, we generated *dia* RNAi embryos that were additionally heterozygous for the kinase-null allele *par-1*^{W3} (Shulman et al., 2000). The combined reduction of Dia and Par-1 worsened metaphase furrow defects versus reduction of either protein individually (Fig. 5, A and B). To test the effect of elevating Par-1 activity, we expressed GFP, GFP–Par-1, or kinase-deficient GFP–Par-1 together with the weaker *dia* shRNA construct. Embryos expressing GFP alone or GFP–Par-1 alone had indistinguishable phalloidin-stained actin bundles in the caps (e.g., for cycle 10 caps, we quantified bundle lengths of 0.971 ± 0.096 µm [mean ± SD; n = 7 embryos] for the former, and 0.977 ± 0.171 µm [mean ± SD; n = 8 embryos] for the latter). *dia* RNAi with coexpression of GFP resulted in minimal phalloidin-stained actin bundles in the caps (Fig. 5, C–E), as observed for the stronger *dia* shRNA construct (Fig. 4). Coexpression of GFP–Par-1 with the weaker *dia* shRNA construct restored the actin bundles, and these bundles were decorated with GFP–Par-1 (Fig. 5 C, arrows; quantified in Fig. 5, D and E), effects that required the kinase activity of Par-1 (Fig. 5, C–E). These genetic interactions show that Par-1 kinase activity promotes the assembly or maintenance of Dia-based actin bundles within a cap, as well as the metaphase compartment that the cap forms. The localization of GFP–Par-1 along the bundles it restores suggests a local effect.

Since kinase-deficient Par-1 (Par-1–KD) was unable to promote proper compartment formation when endogenous Par-1 was depleted (Fig. 1, B and C), we also tested how the construct affected cap actin bundles in this context. RNAi-resistant and kinase-active GFP–Par-1 rescued cap actin bundles of *par-1* RNAi embryos, and the protein localized along rescued bundles (Fig. S4). In contrast, the kinase-deficient construct was unable to rescue cap actin bundles of *par-1* RNAi embryos or to gain a bundle-like localization (Fig. S4). Thus, the Dia-based actin bundles require Par-1 kinase activity.

Par-1 and Dia colocalize along extended regions of the actin bundles separately from Arp3

To test how closely Par-1 and Dia function together, we compared the localization of overexpressed GFP–Par-1, Dia, and F-actin in fixed embryos. During earlier development, the proteins colocalized along actin bundles within the cortical actomyosin network that forms while nuclei divide deep within the embryo (Fig. 6 A, precortical division, arrows; Royou et al., 2002). In forming caps, GFP–Par-1 and Dia colocalized along extended regions of the actin bundles (Fig. 6 A, prophase, arrows). In these fixed samples, their relationship persisted through mitosis with colocalization over the apical surface of caps as well as ingressed furrows (Fig. 6 A; Fig. 9 A shows similar colocalization of endogenously expressed Par-1–GFP with Dia at actin bundles, as well as the specificity of the Dia antibody staining). Examination of cap Arp3-GFP revealed a distinct pattern of numerous small puncta in both live and fixed embryos (Fig. 6, B and C, arrows show co-imaged Dia-positive actin bundles). Thus, Par-1 and Dia colocalize along extended regions of the cap actin bundles, and Arp3 localizes as distinct puncta dispersed among the bundles. Additionally, Par-1 and Dia colocalized at sites along actin bundles of the actomyosin networks, suggesting a relationship in this network as well.

Rho1-GTP is relatively low in the caps and is not promoted by Par-1

Since Rho small G protein activity can relieve formin autoinhibition (Kühn and Geyer, 2014), we examined the localization of Rho1-GTP using a sensor composed of the Rho1-binding domain of Anillin linked to GFP (Munjal et al., 2015). With substantial furrow ingression in control embryos, the sensor strongly labeled the actomyosin borders surrounding each cap, with minimal accumulation in the caps themselves (Fig. 7 A). *RhoGEF2* RNAi depleted the sensor signal in the border (Fig. 7), indicating detection of Rho1-GTP and that RhoGEF2 is a major Rho1 activator in this context, consistent with past studies (Crest et al., 2012).

Next, we assessed the Rho1-GTP sensor in early caps and their surrounding actomyosin borders. At this early stage, Rho1-GTP could be detected with a bundle-like distribution in the caps (Fig. 7 B, arrows), but this detection was substantially lower than that from the actomyosin borders (Fig. 7 B). With ingression, the signal in the caps decreased, while the signal in the borders increased (Fig. 7 B). To test if Par-1 promotes these detections of Rho1-GTP, we made the same comparisons for *par-1* RNAi embryos and observed no decrease in the Rho1-GTP signal in either the caps or their borders (Fig. 7 B). In the *par-1* RNAi embryos, the Rho1-GTP sensor displayed an altered distribution pattern in both cortical domains and somewhat higher levels than controls, effects that might be the result of the cytoskeleton disorganization of these embryos. Thus, Par-1 does not appear to promote

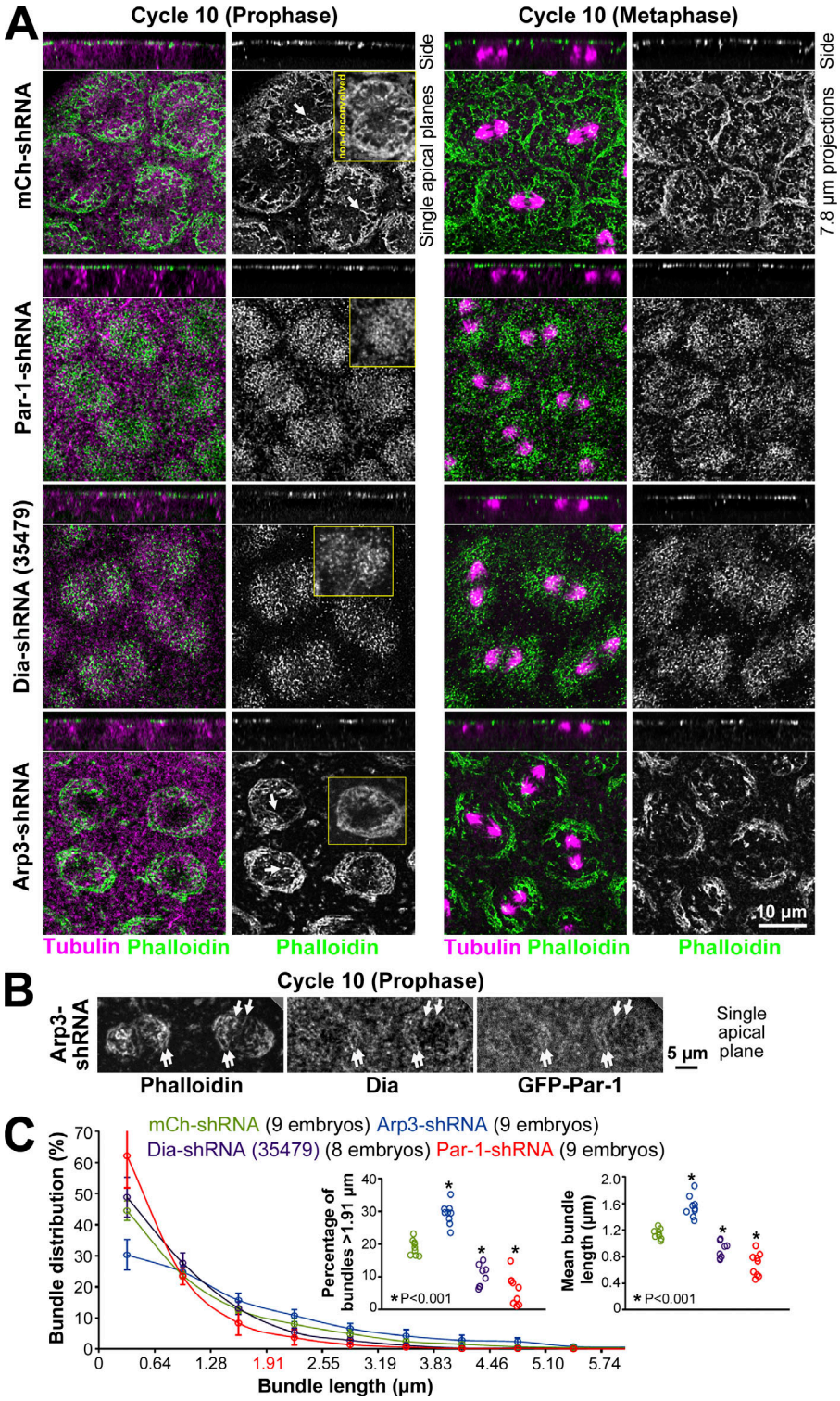

Figure 4. **Par-1 and Dia promote cap actin bundles, and Arp3 promotes a separate cap actin network. (A)** Tubulin staining shows cell cycle stage (note spindles). Phalloidin shows F-actin. Control mCherry RNAi caps show a combination of punctate and bundle-like F-actin (arrows) at prophase. Both pools persist to metaphase with many bundles then around the cap periphery. *par-1* or *dia* RNAi caps display only punctate F-actin and no bundles at both stages. *Arp3* RNAi caps dominated by actin bundles at both stages (arrows). Images deconvolved (squares show the detection of actin bundles and puncta in single caps without deconvolution). **(B)** Dia and GFP–Par-1 (expressed from a UAS construct) in *Arp3* RNAi caps. Arrows indicate phalloidin-stained actin bundles. **(C)** Actin bundle quantifications for cycle 10 prophase of the embryo numbers and genotypes indicated. Asterisks indicate significant differences versus control RNAi.

Rho1 activation. Also, relatively little Rho1-GTP is detected in the caps where Par-1 helps establish or maintain Dia-based actin bundles.

Par-1 organizes Dia in the caps, whereas RhoGEF2 and Rok primarily affect myosin

To test if Par-1 affects Dia localization, we examined endogenous Dia by immunofluorescence in *par-1* RNAi embryos (Fig. 8). Side views of control and *par-1* RNAi embryos revealed cortical Dia enrichment in each case. In top views, control RNAi embryos displayed enrichment of Dia along actin bundles in forming caps (Fig. 8, arrows), both over their apical surface and around their outer circumference. In contrast, *par-1* RNAi embryos displayed a punctate Dia distribution that extended across the disorganized caps and smoothly into the surrounding actomyosin borders. Thus, Dia can be

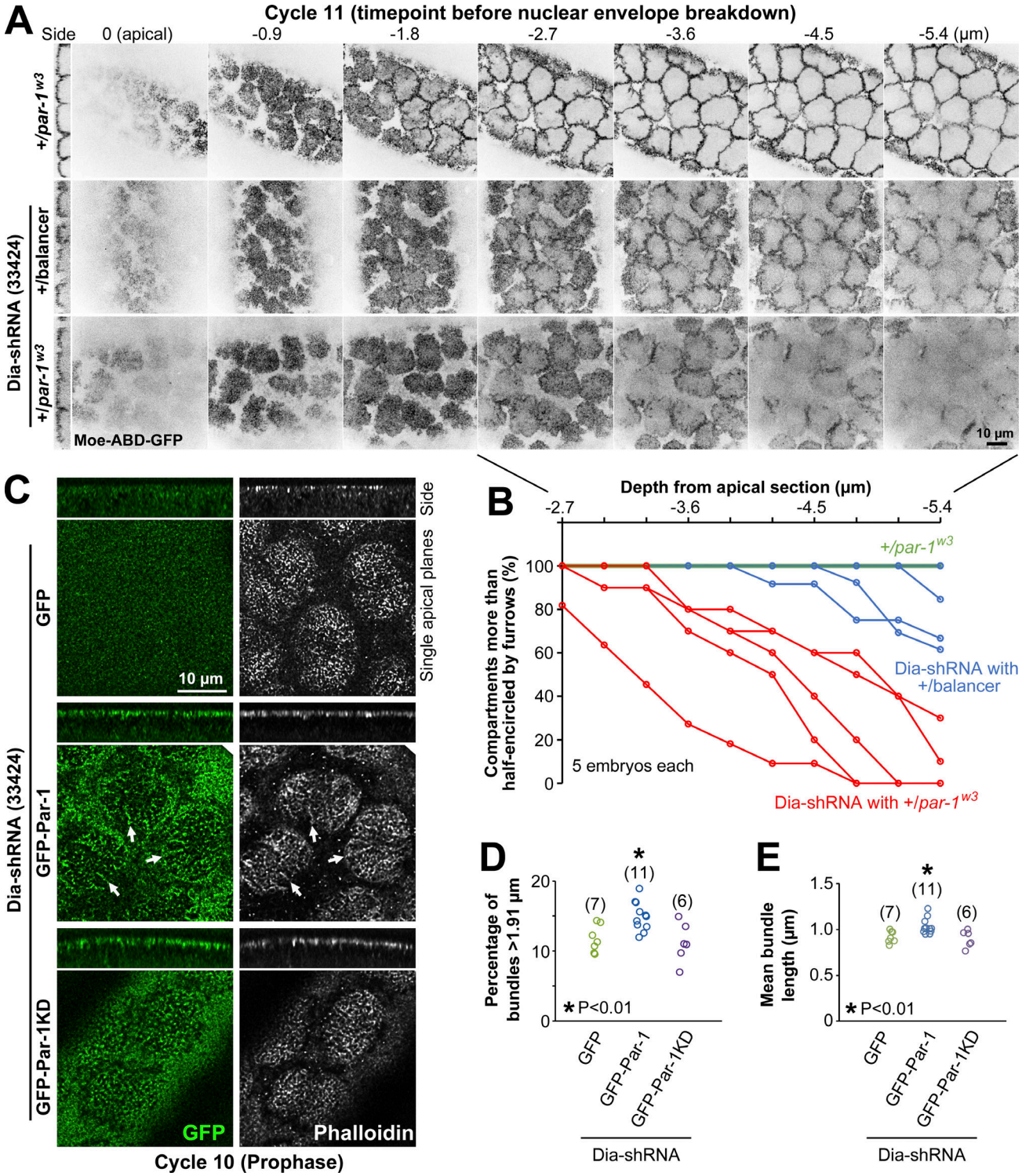

Figure 5. ***dia* RNAi defects can be modified by decreasing or increasing Par-1 kinase activity. (A and B)** Heterozygosity for the kinase-null allele *par-1*^{w3} has no furrow effects (top). For embryos expressing a weaker *dia* shRNA construct, *par-1*^{w3} heterozygosity enhanced furrow defects relative to sibling embryos heterozygous for a balancer chromosome (quantified in B as in Fig. S3 A). **(C)** Embryos expressing the weaker *dia* shRNA constructs display only punctate cap F-actin with GFP coexpression, bundle-like (arrows) plus punctate cap F-actin with GFP–Par-1 coexpression, and only punctate cap F-actin with coexpression of Par-1–KD. Both Par-1 constructs localize to the cortex. The active Par-1 construct is enriched along actin bundles (arrows). Images deconvolved. **(D and E)** Actin organization quantified as in Fig. 4 C (embryo numbers indicated). Asterisks indicate significant differences versus GFP control.

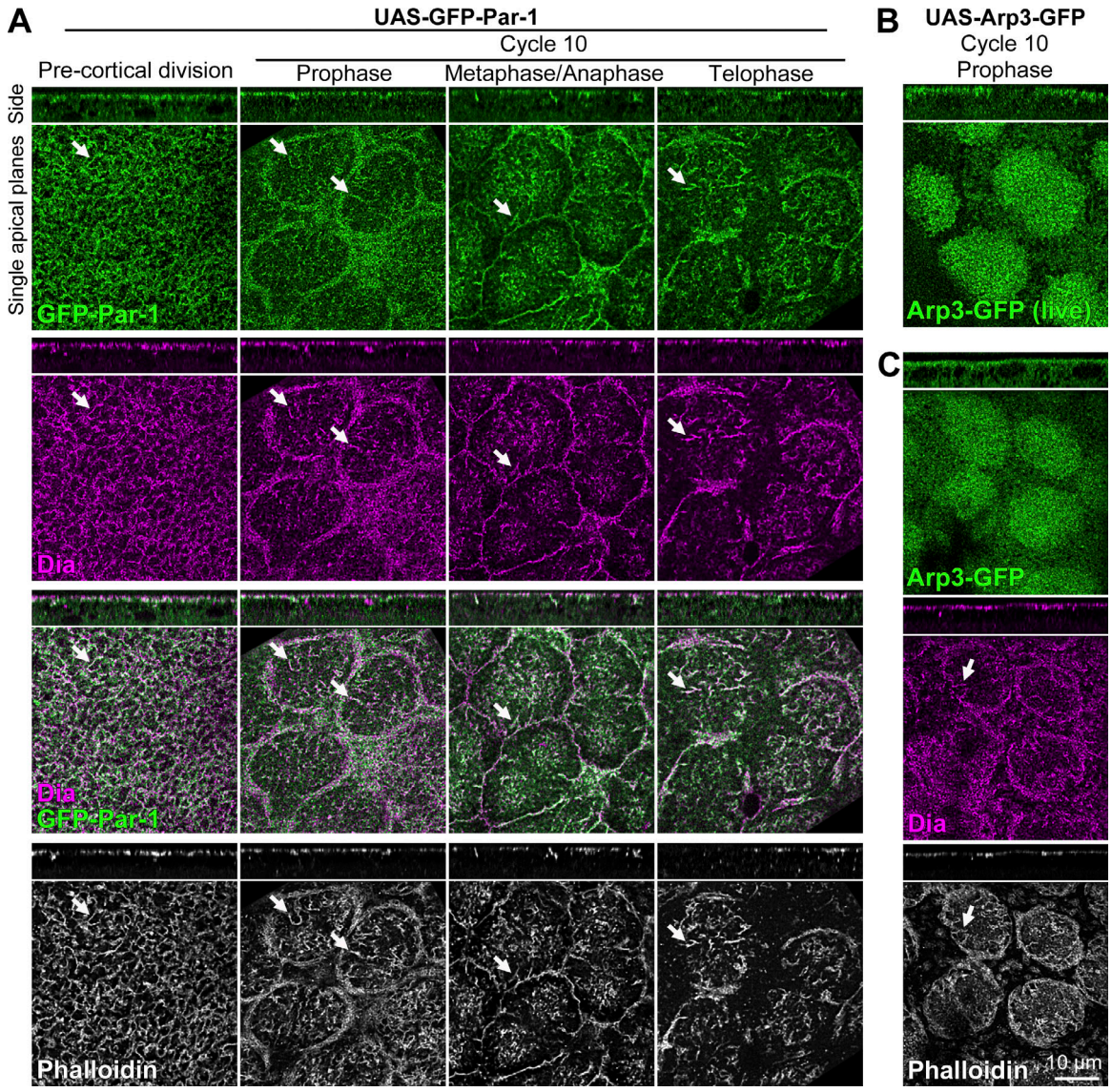

Figure 6. **Par-1 and Dia colocalize along extended regions of actin bundles, and Arp3 has a punctate cortical distribution. (A)** Dia and phalloidin staining of embryos overexpressing GFP–Par-1. Before nuclear division at the embryo cortex, GFP–Par-1, Dia, and F-actin colocalize at bundles (arrows) of the broad, cap-free cortical network. At cycle 10, caps arise and GFP–Par-1, Dia, and F-actin colocalize at bundles at their apical surface (arrows) and at ingressing furrows. **(B)** Overexpressed Arp3-GFP puncta across the apical cap surface live. **(C)** Overexpressed Arp3-GFP puncta without enrichment at Dia-positive bundles (arrow) after fixation. **(A–C)** Images deconvolved.

recruited to the cortex with Par-1 RNAi but fails to organize with actin bundles.

Since binding by Rho1/A and phosphorylation by Rok have each been implicated in formin activation (Kühn and Geyer, 2014), we assessed Dia localization with RNAi depletion of RhoGEF2 or Rok. In each case, Dia was recruited to the cortex, and its organization within the caps resembled control RNAi embryos more than *par-1* RNAi embryos (Fig. 8). Phalloidin-stained actin cap bundles were also readily apparent with each depletion (Fig. 8, arrows; for cycle 10 caps, quantified bundle lengths were similar: 0.944 ± 0.124 µm, 0.831 ± 0.090 µm, and 0.952 ± 0.328 µm [means ± SD] for control RNAi [n = 7 embryos], *RhoGEF2* RNAi [n = 8 embryos], and *Rok* RNAi [n = 9 embryos], respectively). Both the *RhoGEF2* RNAi embryos and the *Rok* RNAi embryos displayed loss of cortical Zip-GFP, a loss not observed with *par-1* RNAi (Fig. 8; note that *par-1* RNAi did affect myosin organization). Thus, RhoGEF2 and Rok have a stronger effect on myosin recruitment than on Dia localization and activity, whereas Par-1 has a stronger effect on Dia, an effect that may, in turn, impact myosin organization.

Dia and F-actin organize Par-1 in the caps

Par-1 could form a prepattern for the Dia-based actin bundles, or the relationship among Dia, Par-1, and actin could be self-organizing. To distinguish these possibilities, we examined how Dia affects the localization of endogenously expressed Par-1–GFP. In control RNAi embryos, the Par-1–GFP localized to Dia-positive actin bundles of the caps (Fig. 9 A, arrows). In

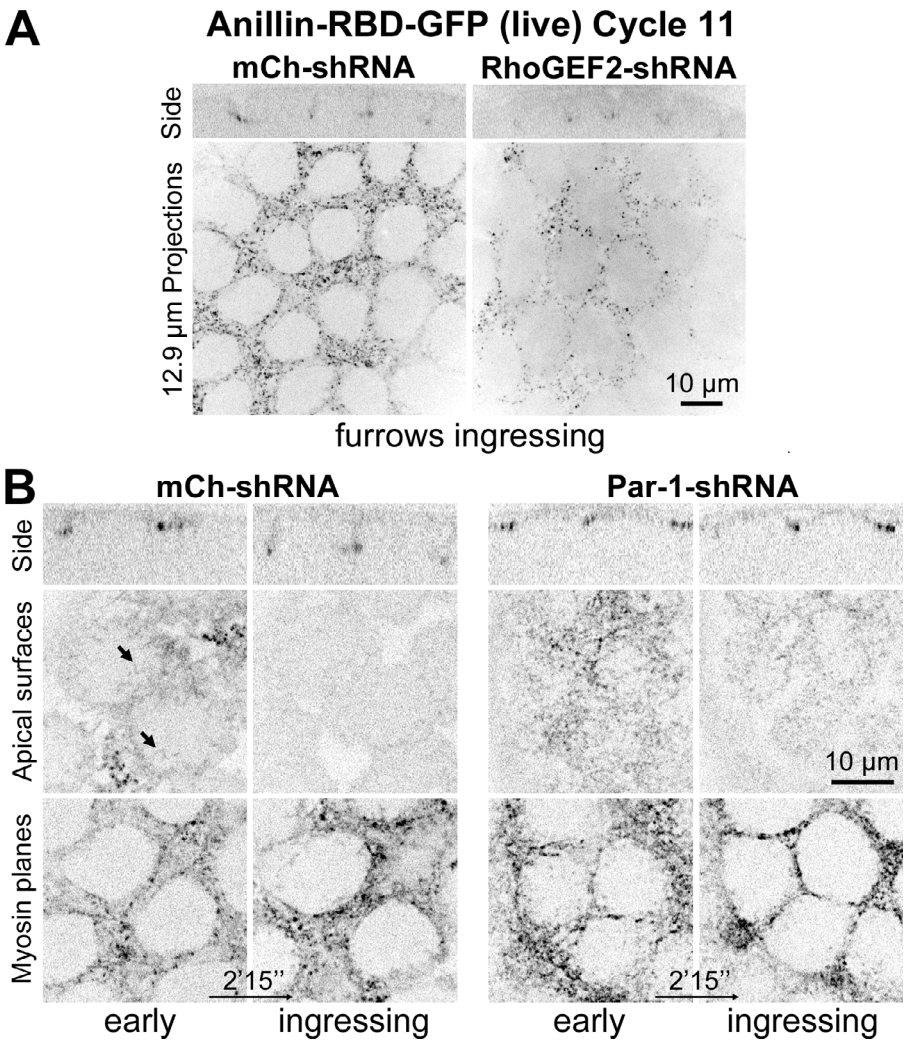

Figure 7. **A Rho1-GTP sensor localizes minimally to caps and is not promoted by Par-1. (A)** The Rho1-GTP sensor Anillin-RBD-GFP enriched at actomyosin borders of control embryos, and with *RhoGEF2* RNAi (observed in 15/15 control RNAi embryos and 12/14 *RhoGEF2* RNAi embryos [combined data of two shRNA constructs] at cycle 11). **(B)** Rho1-GTP sensor detected at bundle-like structures of early caps (arrows) in controls, but its levels were higher in actomyosin borders. With furrow ingression, signal reduced in caps and increased in actomyosin borders. *par-1* RNAi did not diminish the Rho1-GTP sensor signal (observed in 5/5 *par-1* RNAi embryos compared with the controls). With *par-1* RNAi, the sensor signal seemed spatially disorganized and elevated. Time = 0 is arbitrary. Genotypes begin at the same stage. Time given in minutes and seconds.

contrast, *dia* RNAi embryos displayed diffuse cortical Par-1–GFP, a loss of the actin bundles, and strongly diminished Dia staining (Fig. 9 A, side views show the cortical recruitment of Par-1 with both control and *dia* RNAi). Since the actin bundles require both Dia and Par-1, and Dia and Par-1 depend on each other for their bundle-like localization, it seems that these structures form through self-reinforcement. To further test the role of F-actin, we injected embryos with the inhibitor Latrunculin A and examined the live localization of endogenously expressed Par-1–GFP. With carrier control, Par-1–GFP displayed a bundle-like distribution in the caps (Fig. 9 B, white arrows) and also localized to the centrosomes below each cap (Fig. 9 B, yellow arrows). With Latrunculin A, the bundle-like cap distribution was lost (Fig. 9 B), but centrosome localization remained (Fig. 9 B, yellow arrows). Together, these data indicate that the bundle-like localization of Par-1 in the caps depends on both Dia and F-actin.

Arp2/3 is required for displacements of Dia-based actin bundles from each other and toward the cap circumference

To better understand how the Dia-based bundles could contribute to cap growth and metaphase compartment formation, we live-imaged Moe-ABD–GFP with finer time resolution and dissected individual confocal sections during cap growth. In addition to a diffuse distribution of puncta at the apical-most sections (Fig. S5 A), we noticed probe-enriched bundles at the base of folds within subapical sections of the medial region of early cycle caps (Fig. 10 A, purple asterisks; and Fig. S5 A). The numbers of these medial cap bundles increased between telophase and prophase and decreased between prophase and metaphase (Fig. S5 B). *dia* RNAi embryos displayed only the puncta (Fig. 10 B and Fig. S5 A), indicating the ability to detect Dia-based bundles live in the wild-type background. Thus, we monitored bundle behavior with cap growth and furrow ingression. We observed centrifugal bundle displacement with cap growth (Fig. 10 A, green dots) and that distances between bundles increased with cap growth (Fig. 10 A, double-headed arrows; and Video 4). These displacements moved bundles from the cap center into metaphase furrows, and simultaneously the apical cap surface flattened (Fig. 10 A, side views). We hypothesized that the bundle displacements could be due to growth of the intervening Arp2/3 cap networks, or to pulling forces from the actomyosin border surrounding the cap. The bundles formed with *Arp3* RNAi, but did so closer to the cap circumference. Strikingly, central folds were infrequent within these caps (Fig. 10 C, side views; and Fig. S5 A), and over time the bundles often collapsed toward the center of the cap (Fig. 10 C, purple

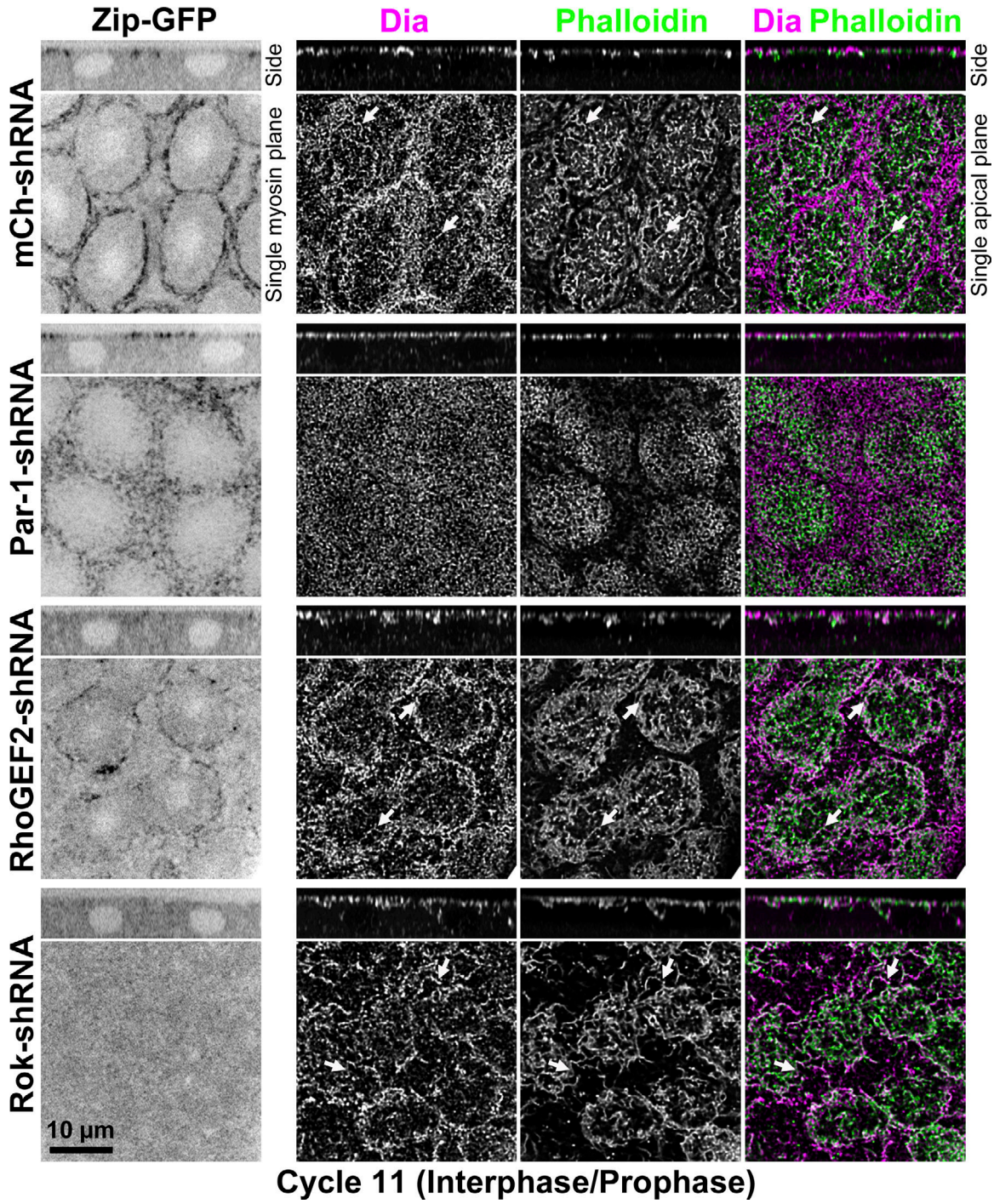

Figure 8. **Par-1 is required for both Dia and actin to form cap bundles, whereas RhoGEF2 and Rok mainly promote myosin at the borders.** Dia and phalloidin staining in embryos endogenously expressing Zip-GFP. Zip-GFP recruited to actomyosin borders of control and *par-1* RNAi embryos (note disorganization with *par-1* RNAi). Dia and F-actin are cortical in *par-1* RNAi embryos but form cap bundles of controls (arrows). Observed in 16/16 control RNAi embryos and 8/8 *par-1* RNAi embryos at cycle 11. For *RhoGEF2* RNAi embryos and *Rok* RNAi embryos, Zip-GFP was lower in borders versus control. Caps of *RhoGEF2* RNAi embryos and *Rok* RNAi embryos displayed Dia-positive actin bundles (arrows). Note the general disorganization of the *Rok* RNAi caps. Observed in 16/16 *RhoGEF2* RNAi embryos (combined data of two shRNA constructs) and 14/14 *Rok* RNAi embryos at cycle 11. Dia and phalloidin images deconvolved.

dots). In contrast, *zip* RNAi embryos displayed bundles that localized to the base of central cap folds (Fig. 10 D and Fig. S5 A) and were displaced from each other and to the cap circumference (Fig. 10 D, double-headed arrows and green dots) as metaphase furrows formed and the apical cap surface flattened (Fig. 10 D, side views). Although the bundles displayed normal behaviors, the caps of *zip* RNAi embryos were abnormally shaped and mispositioned over the embryo surface, consistent with reported effects of myosin depletion (Royou et al., 2002; Zhang et al., 2018). Thus, Arp2/3 is required for (1) central folding of

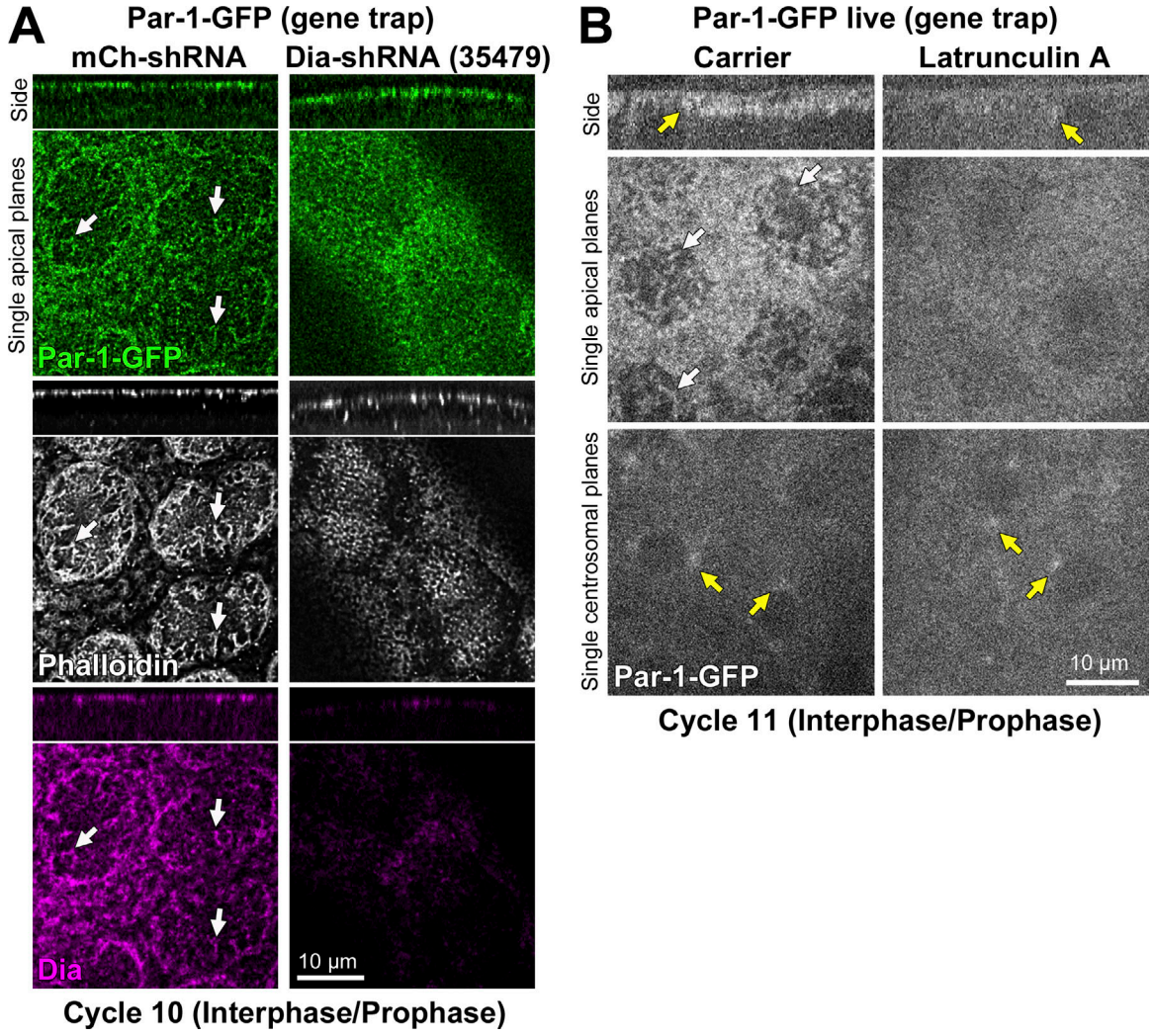

Figure 9. **Dia and F-actin are both required for a bundle-like distribution of Par-1. (A)** Control or *dia* RNAi in embryos expressing endogenous Par-1–GFP and stained with phalloidin and Dia antibodies. In control caps, Par-1–GFP at Dia-positive actin bundles (arrows). In *dia* RNAi caps, Par-1–GFP and F-actin were cortical but bundles were not detected, and Dia was minimally detected. Observed in 12/12 control embryos and 13/13 *dia* RNAi embryos at cycles 10 and 11. Images deconvolved (except for Dia staining). **(B)** Effects of Latrunculin A or carrier injection on endogenous Par-1–GFP in live embryos. Par-1–GFP–positive bundles (white arrows) were observed in carrier control caps, but not Latrunculin A caps. Par-1–GFP–positive centrosomes were observed in both cases (yellow arrows). Observed in 7/7 controls and 6/6 Latrunculin A–injected embryos at cycles 11 and 12.

the cap in proximity to Dia-based bundles, and (2) displacing bundles away from each other and toward the cap circumference as the metaphase compartment forms.

Discussion

Our data reveal a previously unrecognized connection between two well-characterized components of the cell cortex: the formin Dia and the kinase Par-1. Par-1 kinase activity is required for Dia-based actin bundles of a composite material that rounds the cell cortex into dome-shaped metaphase compartments of the syncytial *Drosophila* embryo. Dia and Par-1 closely colocalize along extended regions of the actin bundles, and these bundles, as well as the bundle-like localization of Dia or Par-1, are lost with depletion of either protein, suggesting a self-reinforcing system. These data indicate the importance of Par-1 for the establishment or maintenance of Dia-based actin bundles in the actin cap, a cortical domain with weaker Rho1 signaling than the neighboring actomyosin border. Our localization and genetic studies further indicate that the composite material of the cap forms from separately assembled Dia-based bundles and Arp2/3-based networks. With cap growth, the bundles are displaced away from each other and toward the cap edge through an Arp2/3-dependent mechanism. We propose that the bundles capture pushing forces from interspersed Arp2/3 networks for effective cap growth and compartment formation (Fig. 10 E).

The discovery of a Dia–Par-1 connection adds to a small list of mechanisms that together explain how actin networks are organized for metaphase compartment formation in the syncytial *Drosophila* embryo. Previously characterized mechanisms are (1) a RhoGEF2-Rho-GTP-Rho kinase pathway that promotes myosin assembly around each cap (Crest et al., 2012; Royou et al., 2004) and (2) a Sponge Rac-GEF-Rac-GTP-Scar pathway that induces Arp2/3-based actin polymerization within each cap

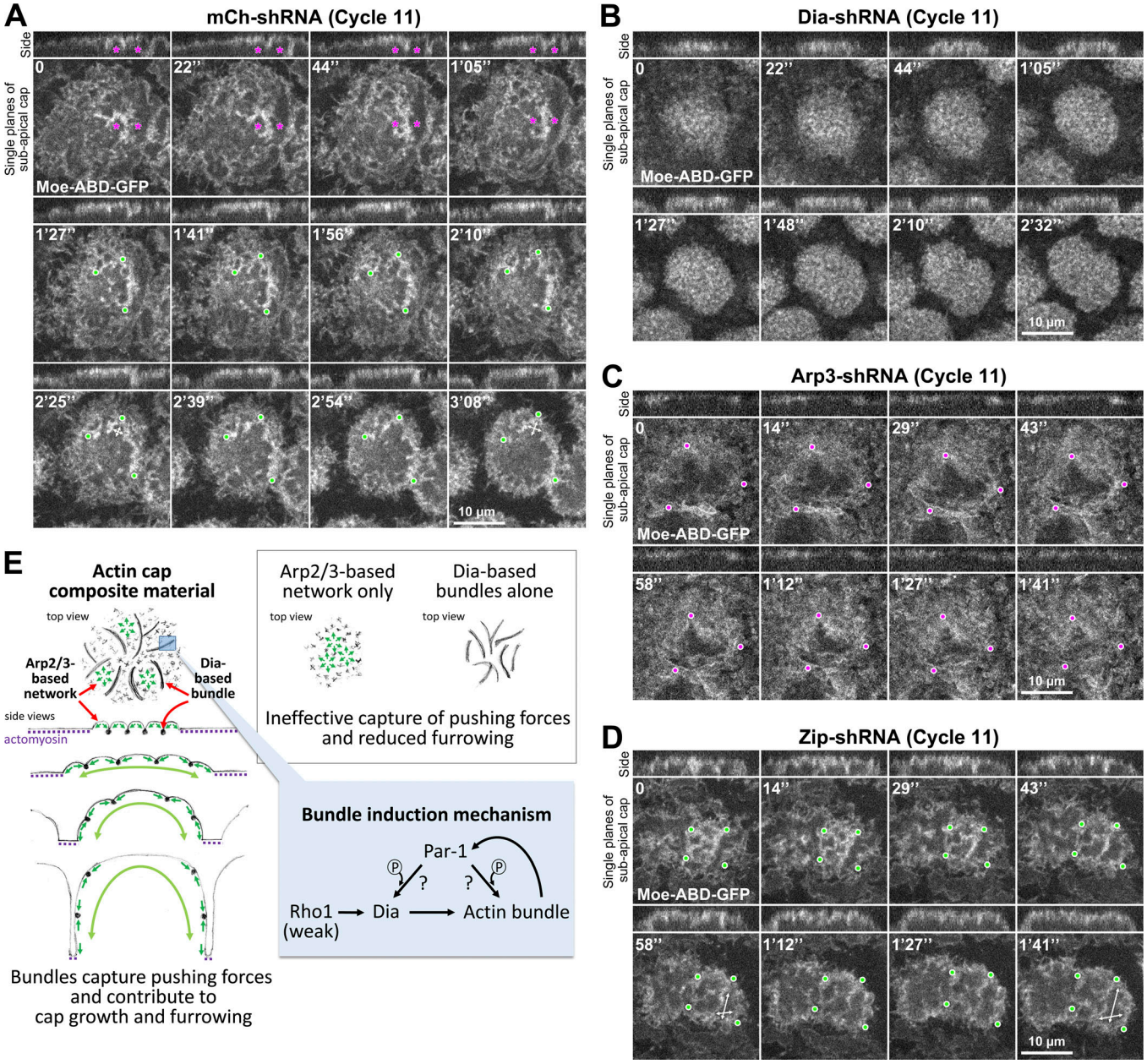

Figure 10. **Arp2/3 is required for displacing actin bundles away from each other and toward the cap circumference. (A–D)** Moe-ABD–GFP in single cycle 11 caps. Time = 0 is arbitrary. Genotypes begin at the same stage. **(A)** In control RNAi during early cap growth, strongest bundle-like signal is observed just below apical cap surface at the base of cap folds (top row; purple asterisks at either side of a bundle in side and surface views). Bottom two rows show bundle displacements away from each other (double-headed arrows) and to cap circumference (green dots). At final time point, apical cap is flattened and largely devoid of bundles. Observed in 7/7 embryos. **(B)** With *dia* RNAi, Moe-ABD–GFP only labeled puncta across the cap. Bundles not detected. Observed in 7/10 embryos (3/10 had fragmented bundles). **(C)** With *Arp3* RNAi, bundles detected but not associated with folds (side views) and collapsed toward the cap center over time (purple dots). 7/10 embryos lacked folds. Bundles collapsed in 5/10 embryos. No bundle movement in 3/10 embryos. Centrifugal bundle displacement in 2/10 embryos. **(D)** With *zip* RNAi, bundles associated with folds (side views) displaced from each other (double-headed arrows) and toward cap circumference (green dots). Note abnormal overall cap shape. Observed in 5/5 embryos. **(E)** Model of bundle induction mechanism and how bundles might function as part of a composite material for metaphase compartment formation (see Discussion). Time given in minutes and seconds.

(Postner et al., 1992; Stevenson et al., 2002; Zallen et al., 2002; Zhang et al., 2018). In addition, Par-1 promotes the establishment or maintenance of Dia-based actin bundles in each cap. Par-1 may also contribute to Dia-based bundles in the actomyosin borders, since the proteins colocalize at these bundles (Fig. 6), and are also required for border myosin organization (Videos 1, 2, and 3; Afshar et al., 2000). However, several observations indicate that the Dia–Par-1 connection in the caps is more relevant to metaphase compartment formation. First, our live-imaging analyses identified defects in cap growth and compartment formation at cortical division cycles preceding strong myosin disorganization. Second, myosin activity is

dispensable for metaphase furrows (Royou et al., 2004; Zhang et al., 2018), and increased actomyosin activity leads to a distinct abnormality of furrow architecture (Lee and Harris, 2013; Zhang et al., 2018). Third, although depletion of Dia or Par-1 led to similar cap and metaphase compartment disruption, the Dia depletion had a stronger, later effect on the bordering myosin (Videos 1, 2, and 3). Compared with the caps, Dia-based F-actin in the actomyosin borders may rely more heavily on the high level of Rho1-GTP detected in these cortical domains.

Like the GEF activities of RhoGEF2 and Sponge, the kinase activity of Par-1 provides an essential signal for cortical effects. However, Par-1 does not simply form an upstream template for bundle organization. Since the bundle-like distribution of Par-1 depends on both Dia and F-actin, and the Dia-based bundles depend on Par-1, a self-reinforcing mechanism seems to organize these assemblies. The colocalization of Dia and Par-1 at long stretches of the bundles suggests an arrangement of many overlapping actin polymers with staggered Dia-decorated growing ends (Skau and Waterman, 2015), a structure that could, in principle, contribute to self-reinforcement through side-to-side stabilization. Whether Par-1 acts upstream or downstream of Dia-based actin polymerization is unclear. Par-1 phosphorylation events could help activate Dia, or could promote the stability of polymers produced (via an actin cross-linker, for example). Determining Par-1 phosphorylation targets and its mechanism of actin association will clarify how the bundles form. Notably, our data do not exclude a role for Rho1 in forming the Dia-based actin bundles of the caps, and indeed, Rho1 inhibitor injection reduces cap growth (Cao et al., 2010). It is possible that Par-1 could help Rho1 relieve Dia autoinhibition (Chen et al., 2017; Higashi et al., 2010), or that Par-1 could promote the bundling and/or stabilization of actin filaments induced by Rho1 and Dia. Either mechanism would be particularly important for Dia-based actin bundles in the cap, where, based on the distributions of the Rho1-GTP sensor (Fig. 7) and the Rho1-GTP effectors Rho kinase and Anillin (Field and Alberts, 1995; Zhang et al., 2018), Rho1-GTP seems to be much less abundant than in the surrounding actomyosin border.

Our data indicate that Dia-based actin bundles and more disperse Arp2/3-based actin networks are required in combination for actin caps to grow and bend inward for metaphase compartment formation. Each network can form with substantial independence, as Dia- or Par-1–depleted caps display mainly diffuse actin networks resembling the normal localization of Arp3-GFP, and Arp3-depleted caps display mainly actin bundles positive for Dia and Par-1. Similar to the actin bundle formation mechanism, the Sponge Rac-GEF-Rac-GTP-Scar-Arp2/3 pathway also displays evidence of self-reinforcement, as cortical Sponge does not accumulate to its wild-type potential when Arp3 is depleted (Zhang et al., 2018). Thus, two self-reinforcing networks may assemble in concert for the growth of an actin cap into a metaphase compartment. Importantly, both Dia and Arp2/3 are needed for this growth. The total amount of actin produced by both mechanisms would presumably contribute, but it is also important to consider the physical properties of the composite material produced. Intriguingly, a recent study of the mouse embryonic stem cell cortex found that both Arp2/3 and formin activities contributed to the cortical network, and that formin inhibition resulted in a denser cortical actin network that was Arp2/3 based and softer than normal (Xia et al., 2019). Thus, the induction, growth, and intermixing of Arp2/3-based networks alone may produce a soft cap incapable of physically engaging its actomyosin border for metaphase compartment formation. The mouse embryonic stem cell cortex displayed a structure of "aster-like" Arp2/3-based networks that seemed to emanate formin-based filaments (Xia et al., 2019). Intriguingly, Arp3 and the Arp2/3-based actin networks of the caps were detected as puncta that might represent such asters. In contrast, the Dia-based actin filaments of the caps were organized as prominent, distinct bundles. These bundles may stiffen the cap cortex further, since bundles are more rigid than single actin filaments in vitro (Bretscher, 1981; Takatsuki et al., 2014). Additionally, we found the bundles to localize to the base of folds within the cap, and to move away from each other and toward the cap circumference in an Arp2/3-dependent, but myosin-independent, process, coupled with cap growth and compartment formation. We propose that Arp2/3 network polymerization pushes against neighboring Dia-based bundles, leading to local folding (micro-buckling) within the cap and then growth of the overall cap against its actomyosin borders for compartment formation (Fig. 10 E). Inflation of an air mattress provides an analogy: air pressure within each partition of the mattress pushes against each partition's boundaries, and, via the boundaries, the multiple partitions push against each other for overall mattress structure. How the proposed micro-buckling would transition into displacements of the bundles and flattening of the cap is unclear, but could involve coupling with biosynthetic mechanisms for plasma membrane growth (Frescas et al., 2006; Holly et al., 2015; Rodrigues et al., 2016), and possibly with physical swelling of the cap (Zhang et al., 2018). Another complexity is the continual turnover of the actin networks. Fluorescence recovery after photobleaching studies show that most cap actin has a half-time of ∼20 s (Cao et al., 2010), and our live imaging of actin bundles revealed continual structural alterations. Also, microvilli-like projections exist on the cap surface, but their abundance seems relatively low at earlier cortical division cycles (Fig. S5 A; Turner and Mahowald, 1976).

The discovery of a Dia–Par-1 relationship also has implications for cell polarity and epithelial morphogenesis. At the end of cellularization, aPKC normally excludes Par-1 from the apical domain (Jiang et al., 2015) and could thereby polarize its effects on Dia-based actin bundles to the basolateral domain. In addition, aPKC antagonizes actomyosin activity in a number of contexts (David et al., 2010; Ishiuchi and Takeichi, 2011; Röper, 2012). aPKC phosphorylation and inhibition of Rho kinase is one identified mechanism (Ishiuchi and Takeichi, 2011). Our work suggests another: aPKC phosphorylation and inhibition of Par-1. We speculate that Par-1 might promote Dia-based actin networks for supporting or remodeling the basolateral domain, while other factors could simultaneously promote established Dia functions in the apicolateral and apical domains (Homem and Peifer, 2008; Levayer et al., 2011; Mason et al., 2013; Massarwa et al., 2009; Mulinari et al., 2008). A repertoire of factors could deploy Dia-based actin networks to various cortical

domains for full control of cell shape. Whether Par-1 and formins function together in other animals will also be important to address.

Materials and methods

A list of resources is provided in Table 1.

Molecular biology and transgenics

The *par-1* coding sequence was PCR amplified for the Par-1 isoform N1S using the cDNA and primers listed in Table 1 and cloned into the pENTR vector using BamHI and XhoI restriction sites. To create the RNAi-resistant *par-1* construct, eight nucleotides within the target region of the *par-1* shRNA were replaced without changing the encoded protein sequence (changing 5′-TAGTTAAATTGTTCCAAGTAA-3′ to 5′-TCGTCA AGCTATTTCAGGTTA-3′) using a synthesized 831-bp fragment (GenScript) and SacI and MluI restriction sites. To create the *par-1* construct encoding Par-1–KD, two amino acid residues important for kinase activity (T408 and S412; Vaccari et al., 2005) were mutated by site-directed mutagenesis (primers in Table 1). Site-directed mutagenesis was performed as previously described (McKinley et al., 2012).

The *mbs* coding sequence was PCR amplified for the Mbs-PI isoform using the cDNA and primers listed in Table 1 and cloned into the pENTR vector using EcoRI and NotI restriction sites. Site-directed mutagenesis created the construct encoding non-phosphorylatable Mbs (Mbs^{T506A}; Majumder et al., 2012) using primers in Table 1.

Gateway cloning (Invitrogen) recombined pENTR constructs into pPGW vectors for N-terminal EGFP tagging (for Par-1 constructs), or into pPWG for no EGFP tagging (for Mbs constructs), downstream of the UASp promoter. Both destination vectors contained an attb recombination site at their Nsi1 site. For transgenic flies, the Par-1 constructs were targeted to the attp40 recombination site on chromosome 2, and Mbs constructs were targeted to the attp2 recombination site on chromosome 3 (BestGene). Flies homozygous for the insertions were generated and maintained, and the insertions were confirmed by PCR and sequencing.

Drosophila husbandry and genetics

Animals were maintained under standard conditions. True breeding stocks were maintained at RT, 18°C, or 25°C on fly food provided by a central University of Toronto kitchen operated by H. Lipshitz. Embryos were collected on plates of apple juice agar (25 g agar, 250 ml store-bought apple juice, 12.5 g store-bought white sugar, 10 ml 10% Tegosept [in ethanol], and distilled H_2O to 1,000 ml) at 25°C after 2–3 d of caged adult feeding on dabs of store-bought baker's yeast, with daily plate changes. Adults were caged for embryo collection within 1 wk of pupal hatching, and no health issues were noticed. Embryo sexes were not determined, and embryo populations with a specific genotype of interest displayed relatively normally distributed phenotypes, suggesting no detectable sex contribution.

UAS constructs were expressed maternally using maternal-α4-tubulin-GAL4-VP16 (mgv), and defects were assessed in offspring. Complex genotypes were synthesized using standard *Drosophila* genetics, and the presence of alleles and transgenes was confirmed after synthesis by probing for expected phenotypes in single-disruption analyses. The synthesized maternal genotypes used in this study are provided in Table 2.

Embryo staining and imaging

For most immunofluorescent staining, embryos were dechorionated with 50% bleach, fixed for 25 min in 1:1 10% formaldehyde/PBS:heptane at 26–28°C, and devitellinized by hand peeling. For staining at cellularization stage, embryos were dechorionated with 50% bleach, fixed for 20 min in 1:1 3.7% formaldehyde/PBS:heptane, and devitellinized by methanol and shaking. Blocking and staining were with PBS/1% goat serum/0.1% Triton X-100. Antibodies and dilutions are listed in Table 1. Fixed and stained embryos were mounted in Aqua Poly/Mount (Polysciences). For phalloidin staining, embryo drying was optimized between the removal of PBS/0.1% Triton X-100 wash solution and the addition of Aqua Poly/Mount.

For live imaging, dechorionated embryos were glued to a coverslip using tape adhesive dissolved in heptane and mounted in halocarbon oil (series 700; Halocarbon Products). The coverslip, with the embryos facing up, was set into the bottom of a glass-bottom culture dish with its original coverslip removed.

Images were collected with a spinning-disk confocal system (Quorum Technologies) at RT with a 63× Plan Apochromat NA 1.4 objective (Carl Zeiss), a piezo top plate, an EM charged coupled device camera (Hamamatsu Photonics), and Volocity software (Quorum Technologies). Z stacks had 300-nm step sizes. Images were analyzed with Volocity software and ImageJ (National Institutes of Health). Images were deconvolved (as indicated in figure legends) using the Volocity Restoration tool with 15 iterations or a confidence of >95% (the first one achieved).

Photoshop and ImageJ were used for figure preparation. Input levels were adjusted so that the main signal range spanned the entire grayscale output. For final figure preparation, some images were resized by bicubic interpolation without noticeable changes at normal viewing magnifications.

Latrunculin A injections

Dechorionated embryos were glued to a coverslip using tape adhesive dissolved in heptane, dehydrated for 14 min at RT, and then mounted in halocarbon oil. Latrunculin A (Sigma-Aldrich) was dissolved in 50% DMSO (Life Technologies) at 500 µM and injected using a Femtotip II needle (Eppendorf) at the embryo anterior or posterior. 50% DMSO was used as the carrier control. Imaging of the central region of the embryo began ∼5 min after the injection.

Postacquisition image analyses

Quantification of phalloidin-stained furrows (Fig. 1 C)

Syncytial embryos were staged at metaphase by spindle morphology seen by tubulin staining. Embryos at cell cycles 11, 12, or 13 were analyzed. Cycle 10 embryos were excluded because their furrows are relatively shallow. Furrow integrity was analyzed with phalloidin staining from 12.9-µm projection views.

Table 1. **Resources used in this study**

Reagent	Source	Number
Antibodies		
Mouse anti–β-tubulin (1:100)	Developmental Studies Hybridoma Bank (DSHB)	DSHB Cat# E7, RRID: AB_528499
Rabbit anti-Dia (1:3,500)	S. Wasserman, University of California at San Diego, La Jolla, CA	N/A
Rabbit anti-Amph (1:1,000)	G. Boulianne, Hospital for Sick Children, Toronto, Ontario, Canada	N/A
Mouse anti-Dlg (1:100)	DSHB	DSHB Cat# 4F3, RRID: AB_528203
Alexa Fluor 568–conjugated phalloidin (1:200)	Invitrogen	Cat# A-12380
Goat anti-mouse Alexa Fluor 568 (1:500)	Invitrogen	Cat# A-11004, RRID: AB_141371
Goat anti-mouse Alexa Fluor 647 (1:500)	Invitrogen	Cat# A-21235, RRID: AB_141693
Goat anti-rabbit Alexa Fluor 488 (1:500)	Invitrogen	Cat# A-11008, RRID: AB_143165
Goat anti-rabbit Alexa Fluor 568 (1:500)	Invitrogen	Cat# A-11011, RRID: AB_143157
Goat anti-rabbit Alexa Fluor 647 (1:500)	Invitrogen	Cat# A-21245, RRID: AB_141775
Mounting reagents		
Aqua Polymount	Polysciences	Cat #18606-5
Halocarbon oil (series 700)	Halocarbon Products	Cat #9002-83-9
***Drosophila* lines**		
Maternal-α4-tubulin-GAL4::VP16	M. Peifer, University of North Carolina at Chapel Hill, Chapel Hill, NC	N/A
UASp-mCherry-shRNA	Bloomington Drosophila Stock Center (BDSC)	BDSC #35785
UASp-Par-1-shRNA	BDSC	BDSC #35342
UASp-Arp3-shRNA	BDSC	BDSC #53972
UASp-Dia-shRNA (33424)	BDSC	BDSC #33424
UASp-Dia-shRNA (35479)	BDSC	BDSC #35479
UASp-RhoGEF2-shRNA (34643)	BDSC	BDSC #34643
UASp-RhoGEF2-shRNA (76255)	BDSC	BDSC #76255
UASp-Rok-shRNA	Zhang et al., 2018	N/A
UASp-Dlg-shRNA	BDSC	BDSC #35286
UASp-Zip-shRNA	BDSC	BDSC #36727
UASp-GFP	U. Tepass, University of Toronto	N/A
UASp-GFP-Par-1	This study	N/A
UASp-GFP-Par-1KD	This study	N/A
UASp-Mbs	This study	N/A
UASp-Mbs^{T506A}	This study	N/A
UASp-Baz-GFP	McKinley et al., 2012	N/A
UASp-Baz^{S151AS1085A}-GFP	Jiang et al., 2015	N/A
UASp-Arp3-GFP	BDSC	BDSC #39722
Anillin-RBD-GFP	T. Lecuit, Developmental Biology Institute of Marseille, France	N/A
Par-1-GFP Trap	Flytrap	CC01981

Table 1. **Resources used in this study (*Continued*)**

Reagent	Source	Number
Zip-GFP Trap	Flytrap	#51564
UASp-mCherry-Tubulin	N. Rusan, National Heart, Lung, and Blood Institute, Bethesda, MD	N/A
ncd-ncd-mRFP	BDSC	BDSC #58372
sqh-Moe-ABD-GFP	D. Kiehart, Duke University, Durham Hill, NC	N/A
par-1^{w3}/Cyo	D. St Johnston, Cambridge University, Cambridge, UK	N/A
Oligonucleotides		
Primers for *par-1* coding region PCR amplification: 5′-CGCGGATCCGATGTCGACAGCAAT GCGCACCACACTGC-3′ (forward) and 5′-CCGCTCGAGTTACTGGTTTGGCCGTTTGCTAAA ACG-3′ (reverse)	Life Technologies	N/A
Primers for site-directed mutagenesis to generate Par-1–KD: 5′-CGCGTTCTGCGGTGC CCCGCCATAT-3′ (forward) and 5′-ATATGGCGGGGCACCGCAGAACGCG-3′ (reverse)	Life Technologies	N/A
Primers for *mbs* coding region PCR amplification: 5′-CAAGAAGGATCTGAATTCATGTCC TCGCTGGACGCA-3′ (forward) and 5′-GTGCGAGTTCGCGGCCGCTCATTTACTTAATTTGC-3′ (reverse)	Life Technologies	N/A
Primers for site-directed mutagenesis to generate Mbs^{T506A}: 5′-CGACGGTCTGCCCAA GGTGTCACCCTG-3′ (forward) and 5′-CAGGGTGACACCTTGGGCAGACCGTCG-3′ (reverse)	Life Technologies	N/A
Recombinant DNA		
Drosophila Par-1 N1S cDNA clone	Drosophila Genomics Resource Center (DGRC)	RE47050
Drosophila Mbs cDNA clone	DGRC	RE63915
pENTR	Invitrogen	Cat# A-10463
pPGW	DGRC	DGRC:1077
Software and algorithms		
Volocity 4.2.1	Quorum Technologies Inc.	N/A
ImageJ	National Institutes of Health	N/A
Ridge Detection 1.4.0	ImageJ plugin	N/A
Adobe Photoshop CS4	Adobe	N/A

Embryos with each mitotic spindle completely surrounded by furrows were categorized as having complete cleavage furrows. Embryos with spindles that were only partially enclosed by furrows were categorized as having broken furrow defects. Embryos in which >50% of spindles did not have any ingressed furrows surrounding them were categorized as having lost furrow defects. Compartments at the middle of each embryo were imaged for analysis.

Quantification of actin caps (Figs. 3 B, S3 A, and S5 B)

To quantify cap growth, embryos at cycle 11 were live imaged. The quantification start point was when actin cap patches began to form in the time point just after nuclear envelope formation. The end point was when caps met neighboring caps or when caps elongated at anaphase (whichever came first, depending on the genotype). Images (8.1 µm projections) were selected at every third time point (every 34.5 s). For each embryo, three caps were randomly selected by the quick selection tool in Photoshop for area measurement over time, and the three cap measurements were averaged to provide a value for one embryo.

To quantify compartment formation, single time point stacks collected just before nuclear envelope breakdown at cycle 11 were analyzed at each z-section. We distinguished compartments as having furrows encircling >50% of the compartment or not. Percentages were then determined based on the total number of compartments determined from the top z-section.

Quantification of myosin-positive furrow depth (Fig. S3 C)

Embryos at cycle 11 were live imaged. Single time point stacks were analyzed just before nuclear envelope breakdown. The length of ingressed furrows was determined by the distance between the top plane where myosin signal just appears and the bottom plane where myosin level at the furrow base becomes lost. The maximum furrow length was determined for each embryo.

Quantification of actin bundles (Figs. 4 C and 5, D and E)

Stacks were deconvolved in Volocity. Single apical-plane images of phalloidin-stained cycle 10 embryos at interphase/prophase were selected and adjusted in Photoshop to fill the grayscale.

Table 2. **Synthesized maternal genotypes used in this study**

Par-1 RNAi rescue experiments
mgv/+; UASp-mCherry(mCh)-shRNA/+
mgv/+; UASp-Par-1-shRNA/+
mgv/+; UASp-GFP-Par-1 (RNAi resistant)/+; UASp-Par-1-shRNA/+
mgv/+; UASp-Par-1KD-GFP (RNAi resistant)/+; UASp-Par-1-shRNA/+
Analyses of known Par-1 phosphorylation targets
mgv/+; Zip-GFP trap/+; UASp-mCh-shRNA/+
mgv/+; Zip-GFP trap/+; UASp-Mbs/+
mgv/+; Zip-GFP trap/+; UASp-Mbs^{T506A}/+
mgv/+; UASp-GFP/+
mgv/+; UASp-Baz-GFP/+
mgv/+; UASp-Baz^{S151AS1085A}-GFP/+
mgv/+; UASp-mCh-shRNA/+
mgv/+; UASp-Dlg-shRNA/+
mgv/+; UASp-Dlg-shRNA/UASp-mCh-shRNA
mgv/+; UASp-Dlg-shRNA/UASp-Par-1-shRNA
Par-1 localization analyses
mgv/+; UASp-GFP-Par-1 (RNAi resistant)/+; UASp-Par-1-shRNA/+
mgv/+; Par-1-GFP trap/+; UASp-mCh-shRNA
mgv/+; Par-1-GFP trap/+; UASp-Dia-shRNA (35479)
Live imaging of cytoskeleton markers
mgv/+; sqh-Moe-ABD-GFP/+; UASp-mCh-shRNA/+
mgv/+; sqh-Moe-ABD-GFP/+; UASp-Par-1-shRNA/+
mgv/+; sqh-Moe-ABD-GFP/UASp-Dia-shRNA (35479)
mgv/+; sqh-Moe-ABD-GFP/UASp-Arp3-shRNA
mgv/+; sqh-Moe-ABD-GFP/+; UASp-Zip-shRNA/+
mgv/+; Zip-GFP trap/+; UASp-mCh-shRNA/+
mgv/+; Zip-GFP trap/+; UASp-Par-1-shRNA/+
mgv/+; Zip-GFP trap/UAS-Dia-shRNA (35479)
mgv; UASp-mCherry-Tubulin
mgv/+; UASp-mCherry-Tubulin/UASp-Par-1-shRNA
mgv/+; ncd-ncd-mRFP/UASp-Par-1-shRNA
Dia, Par-1, Arp3, and F-actin fixed localization studies
mgv/+; UASp-mCh-shRNA/+
mgv/+; UASp-Par-1-shRNA/+
mgv/+; UASp-Dia-shRNA (35479)/+
mgv/+; UASp-Arp3-shRNA/+
mgv/+; UASp-GFP-Par-1/+
mgv/+; UASp-Arp3-GFP/+
mgv/+; UASp-GFP-Par-1/UASp-Arp3-shRNA
Dia RNAi enhancement experiments
mgv/+; *par-1*^{w3}/sqh-Moe-ABD-GFP
mgv/+; *par-1*^{w3}/sqh-Moe-ABD-GFP; UASp-Dia-shRNA (33424)/+
mgv/+; Cyo/sqh-Moe-ABD-GFP; UASp-Dia-shRNA (33424)/+ (sibling of line above)

Table 2. **Synthesized maternal genotypes used in this study (*Continued*)**

Par-1 RNAi rescue experiments
Dia RNAi suppression experiments
mgv/+; UASp-GFP/UASp-Dia-shRNA (33424)
mgv/+; UASp-GFP-Par-1 (RNAi resistant)/+; UASp-Dia-shRNA (33424)/+
mgv/+; UASp-Par-1KD-GFP (RNAi resistant)/+; UASp-Dia-shRNA (33424)/+
RhoGEF2-Rho1 pathway experiments
mgv/+; Zip-GFP trap/+; UASp-mCh-shRNA/+
mgv/+; Zip-GFP trap/+; UASp-Par-1-shRNA/+
mgv/+; Zip-GFP trap/+; UASp-RhoGEF2-shRNA (34643)/+
mgv/+; Zip-GFP trap/+; UASp-Rok-shRNA/+
mgv/+; Anillin-RBD-GFP/UASp-mCh-shRNA
mgv/+; Anillin-RBD-GFP/UASp-Par-1-shRNA
mgv/+; Anillin-RBD-GFP/UASp-RhoGEF2-shRNA (34643)

Three caps per image/embryo were randomly selected using the quick selection tool in Photoshop and exported to ImageJ. Bundles were automatically identified using ImageJ plugin Ridge Detection 1.4.0 with the following parameters: line width, 0.5; high contrast, 400; low contrast, 100; min-length, 1; add to manager, selected; slope, selected. The length of each bundle was then measured. Bundle length distributions and averages were determined in Excel (Microsoft).

Statistics

Comparisons were done with Student's *t* tests (two tailed, unpaired) using Excel. Means are shown with SDs. Unless noted otherwise, *n* values refer to embryo numbers analyzed in the comparison (see figures and legends).

Online supplemental material

Video 1 shows Zip-GFP in a control mCherry RNAi embryo from cycle 11 to 14. Video 2 shows Zip-GFP in a *par-1* RNAi embryo from cycle 11 to 14. Video 3 shows Zip-GFP in a *dia* RNAi embryo from cycle 11 to 14. Video 4 shows Moe-ABD–GFP in a single cap in a control RNAi embryo at cycle 11. Fig. S1 shows that individual microtubule networks appear unaffected by depletion of Par-1 at early syncytial division cycles, but spindle collisions arise. Fig. S2 shows that the dependence of compartments on Par-1 is not explained by mis-regulation of known Par-1 phosphorylation targets. Fig. S3 shows that depletion of Par-1 or Dia reduces ingression of compartment furrows, but affects myosin modestly at early syncytial division cycles. Fig. S4 shows that without its kinase activity, Par-1 cannot promote actin bundles or localize as bundles. Fig. S5 shows confocal sectioning showing the depths and cell cycle timing of medial cap bundles.

Acknowledgments

We thank A. Wilde and R. Winklbauer for critiquing the manuscript. We thank G. Boulianne, D. Kiehart, T. Lecuit, M. Peifer, N. Rusan, D. St Johnston, U. Tepass, and S. Wasserman for

reagents. We thank Cao Guo Yu for technical assistance. Stocks obtained from the Bloomington Drosophila Stock Center (NIH P40OD018537) were used in this study. Monoclonal antibodies were obtained from the Developmental Studies Hybridoma Bank, created by the National Institute of Child Health of the National Institutes of Health (NIH) and maintained at The University of Iowa. We thank the Drosophila Transgenic RNAi Project and the Flytrap collection for reagents. cDNA clones and vectors were obtained from the Drosophila Genomics Resource Center, supported by NIH grant 2P40OD010949.

The work was supported by Natural Sciences and Engineering Research Council of Canada Discovery grant RGPIN-2016-05617 to T.J.C. Harris, and was part of the University of Toronto's Medicine by Design initiative, which receives funding from the Canada First Research Excellence Fund.

The authors declare no competing financial interests.

Author contributions: T.J.C. Harris and T. Jiang conceptualized the project. T. Jiang generated reagents and conducted the experiments. T.J.C. Harris and T. Jiang analyzed the data. T. Jiang quantified the data. T. Jiang prepared the figures and T.J.C. Harris edited the figures. T.J.C. Harris wrote the manuscript and T. Jiang edited the manuscript.

Submitted: 25 March 2019
Revised: 21 August 2019
Accepted: 22 September 2019

References

Afshar, K., B. Stuart, and S.A. Wasserman. 2000. Functional analysis of the Drosophila diaphanous FH protein in early embryonic development. *Development.* 127:1887–1897.

Bayraktar, J., D. Zygmunt, and R.W. Carthew. 2006. Par-1 kinase establishes cell polarity and functions in Notch signaling in the Drosophila embryo. *J. Cell Sci.* 119:711–721. https://doi.org/10.1242/jcs.02789

Benton, R., and D. St Johnston. 2003. Drosophila PAR-1 and 14-3-3 inhibit Bazooka/PAR-3 to establish complementary cortical domains in polarized cells. *Cell.* 115:691–704. https://doi.org/10.1016/S0092-8674(03)00938-3

Bretscher, A. 1981. Fimbrin is a cytoskeletal protein that crosslinks F-actin in vitro. *Proc. Natl. Acad. Sci. USA.* 78:6849–6853. https://doi.org/10.1073/pnas.78.11.6849

Cao, J., J. Crest, B. Fasulo, and W. Sullivan. 2010. Cortical actin dynamics facilitate early-stage centrosome separation. *Curr. Biol.* 20:770–776. https://doi.org/10.1016/j.cub.2010.02.060

Chen, A., P.D. Arora, C.A. McCulloch, and A. Wilde. 2017. Cytokinesis requires localized β-actin filament production by an actin isoform specific nucleator. *Nat. Commun.* 8:1530. https://doi.org/10.1038/s41467-017-01231-x

Chugh, P., and E.K. Paluch. 2018. The actin cortex at a glance. *J. Cell Sci.* 131: jcs186254.

Crest, J., K. Concha-Moore, and W. Sullivan. 2012. RhoGEF and positioning of rappaport-like furrows in the early Drosophila embryo. *Curr. Biol.* 22: 2037–2041. https://doi.org/10.1016/j.cub.2012.08.046

David, D.J., A. Tishkina, and T.J. Harris. 2010. The PAR complex regulates pulsed actomyosin contractions during amnioserosa apical constriction in Drosophila. *Development.* 137:1645–1655. https://doi.org/10.1242/dev.044107

Doerflinger, H., N. Vogt, I.L. Torres, V. Mirouse, I. Koch, C. Nüsslein-Volhard, and D. St Johnston. 2010. Bazooka is required for polarisation of the Drosophila anterior-posterior axis. *Development.* 137:1765–1773. https://doi.org/10.1242/dev.045807

Field, C.M., and B.M. Alberts. 1995. Anillin, a contractile ring protein that cycles from the nucleus to the cell cortex. *J. Cell Biol.* 131:165–178. https://doi.org/10.1083/jcb.131.1.165

Foe, V.E., and B.M. Alberts. 1983. Studies of nuclear and cytoplasmic behaviour during the five mitotic cycles that precede gastrulation in Drosophila embryogenesis. *J. Cell Sci.* 61:31–70.

Foe, V.E., C.M. Field, and G.M. Odell. 2000. Microtubules and mitotic cycle phase modulate spatiotemporal distributions of F-actin and myosin II in Drosophila syncytial blastoderm embryos. *Development.* 127:1767–1787.

Frescas, D., M. Mavrakis, H. Lorenz, R. Delotto, and J. Lippincott-Schwartz. 2006. The secretory membrane system in the Drosophila syncytial blastoderm embryo exists as functionally compartmentalized units around individual nuclei. *J. Cell Biol.* 173:219–230. https://doi.org/10.1083/jcb.200601156

Goldstein, B., and I.G. Macara. 2007. The PAR proteins: fundamental players in animal cell polarization. *Dev. Cell.* 13:609–622. https://doi.org/10.1016/j.devcel.2007.10.007

Grosshans, J., C. Wenzl, H.M. Herz, S. Bartoszewski, F. Schnorrer, N. Vogt, H. Schwarz, and H.A. Müller. 2005. RhoGEF2 and the formin Dia control the formation of the furrow canal by directed actin assembly during Drosophila cellularisation. *Development.* 132:1009–1020. https://doi.org/10.1242/dev.01669

Higashi, T., T. Ikeda, T. Murakami, R. Shirakawa, M. Kawato, K. Okawa, M. Furuse, T. Kimura, T. Kita, and H. Horiuchi. 2010. Flightless-I (Fli-I) regulates the actin assembly activity of diaphanous-related formins (DRFs) Daam1 and mDia1 in cooperation with active Rho GTPase. *J. Biol. Chem.* 285:16231–16238. https://doi.org/10.1074/jbc.M109.079236

Holly, R.M., L.M. Mavor, Z. Zuo, and J.T. Blankenship. 2015. A rapid, membrane-dependent pathway directs furrow formation through RalA in the early Drosophila embryo. *Development.* 142:2316–2328. https://doi.org/10.1242/dev.120998

Homem, C.C., and M. Peifer. 2008. Diaphanous regulates myosin and adherens junctions to control cell contractility and protrusive behavior during morphogenesis. *Development.* 135:1005–1018. https://doi.org/10.1242/dev.016337

Ishiuchi, T., and M. Takeichi. 2011. Willin and Par3 cooperatively regulate epithelial apical constriction through aPKC-mediated ROCK phosphorylation. *Nat. Cell Biol.* 13:860–866. https://doi.org/10.1038/ncb2274

Jiang, T., R.F. McKinley, M.A. McGill, S. Angers, and T.J. Harris. 2015. A Par-1-Par-3-Centrosome Cell Polarity Pathway and Its Tuning for Isotropic Cell Adhesion. *Curr. Biol.* 25:2701–2708. https://doi.org/10.1016/j.cub.2015.08.063

Kiehart, D.P., C.G. Galbraith, K.A. Edwards, W.L. Rickoll, and R.A. Montague. 2000. Multiple forces contribute to cell sheet morphogenesis for dorsal closure in Drosophila. *J. Cell Biol.* 149:471–490. https://doi.org/10.1083/jcb.149.2.471

Kühn, S., and M. Geyer. 2014. Formins as effector proteins of Rho GTPases. *Small GTPases.* 5:e29513. https://doi.org/10.4161/sgtp.29513

Lang, C.F., and E. Munro. 2017. The PAR proteins: from molecular circuits to dynamic self-stabilizing cell polarity. *Development.* 144:3405–3416. https://doi.org/10.1242/dev.139063

Lawson, C.D., and A.J. Ridley. 2018. Rho GTPase signaling complexes in cell migration and invasion. *J. Cell Biol.* 217:447–457. https://doi.org/10.1083/jcb.201612069

Lecuit, T., P.F. Lenne, and E. Munro. 2011. Force generation, transmission, and integration during cell and tissue morphogenesis. *Annu. Rev. Cell Dev. Biol.* 27:157–184. https://doi.org/10.1146/annurev-cellbio-100109-104027

Lee, D.M., and T.J. Harris. 2013. An Arf-GEF regulates antagonism between endocytosis and the cytoskeleton for Drosophila blastoderm development. *Curr. Biol.* 23:2110–2120. https://doi.org/10.1016/j.cub.2013.08.058

Levayer, R., A. Pelissier-Monier, and T. Lecuit. 2011. Spatial regulation of Dia and Myosin-II by RhoGEF2 controls initiation of E-cadherin endocytosis during epithelial morphogenesis. *Nat. Cell Biol.* 13:529–540. https://doi.org/10.1038/ncb2224

Majumder, P., G. Aranjuez, J. Amick, and J.A. McDonald. 2012. Par-1 controls myosin-II activity through myosin phosphatase to regulate border cell migration. *Curr. Biol.* 22:363–372. https://doi.org/10.1016/j.cub.2012.01.037

Mason, F.M., M. Tworoger, and A.C. Martin. 2013. Apical domain polarization localizes actin-myosin activity to drive ratchet-like apical constriction. *Nat. Cell Biol.* 15:926–936. https://doi.org/10.1038/ncb2796

Massarwa, R., E.D. Schejter, and B.Z. Shilo. 2009. Apical secretion in epithelial tubes of the Drosophila embryo is directed by the Formin-family protein Diaphanous. *Dev. Cell.* 16:877–888. https://doi.org/10.1016/j.devcel.2009.04.010

McDonald, J.A. 2014. Canonical and noncanonical roles of Par-1/MARK kinases in cell migration. *Int. Rev. Cell Mol. Biol.* 312:169–199. https://doi.org/10.1016/B978-0-12-800178-3.00006-3

McKinley, R.F., and T.J. Harris. 2012. Displacement of basolateral Bazooka/PAR-3 by regulated transport and dispersion during epithelial polarization in Drosophila. *Mol. Biol. Cell.* 23:4465–4471. https://doi.org/10.1091/mbc.e12-09-0655

McKinley, R.F., C.G. Yu, and T.J. Harris. 2012. Assembly of Bazooka polarity landmarks through a multifaceted membrane-association mechanism. *J. Cell Sci.* 125:1177–1190. https://doi.org/10.1242/jcs.091884

Mulinari, S., M.P. Barmchi, and U. Häcker. 2008. DRhoGEF2 and diaphanous regulate contractile force during segmental groove morphogenesis in the Drosophila embryo. *Mol. Biol. Cell.* 19:1883–1892. https://doi.org/10.1091/mbc.e07-12-1230

Munjal, A., J.M. Philippe, E. Munro, and T. Lecuit. 2015. A self-organized biomechanical network drives shape changes during tissue morphogenesis. *Nature.* 524:351–355. https://doi.org/10.1038/nature14603

Nishimura, I., Y. Yang, and B. Lu. 2004. PAR-1 kinase plays an initiator role in a temporally ordered phosphorylation process that confers tau toxicity in Drosophila. *Cell.* 116:671–682. https://doi.org/10.1016/S0092-8674(04)00170-9

Postner, M.A., K.G. Miller, and E.F. Wieschaus. 1992. Maternal effect mutations of the sponge locus affect actin cytoskeletal rearrangements in Drosophila melanogaster embryos. *J. Cell Biol.* 119:1205–1218. https://doi.org/10.1083/jcb.119.5.1205

Raff, J.W., and D.M. Glover. 1989. Centrosomes, and not nuclei, initiate pole cell formation in Drosophila embryos. *Cell.* 57:611–619. https://doi.org/10.1016/0092-8674(89)90130-X

Riechmann, V., and A. Ephrussi. 2004. Par-1 regulates bicoid mRNA localisation by phosphorylating Exuperantia. *Development.* 131:5897–5907. https://doi.org/10.1242/dev.01515

Riechmann, V., G.J. Gutierrez, P. Filardo, A.R. Nebreda, and A. Ephrussi. 2002. Par-1 regulates stability of the posterior determinant Oskar by phosphorylation. *Nat. Cell Biol.* 4:337–342. https://doi.org/10.1038/ncb782

Rodrigues, F.F., W. Shao, and T.J. Harris. 2016. The Arf GAP Asap promotes Arf1 function at the Golgi for cleavage furrow biosynthesis in Drosophila. *Mol. Biol. Cell.* 27:3143–3155. https://doi.org/10.1091/mbc.e16-05-0272

Röper, K. 2012. Anisotropy of Crumbs and aPKC drives myosin cable assembly during tube formation. *Dev. Cell.* 23:939–953. https://doi.org/10.1016/j.devcel.2012.09.013

Royou, A., W. Sullivan, and R. Karess. 2002. Cortical recruitment of nonmuscle myosin II in early syncytial Drosophila embryos: its role in nuclear axial expansion and its regulation by Cdc2 activity. *J. Cell Biol.* 158:127–137. https://doi.org/10.1083/jcb.200203148

Royou, A., C. Field, J.C. Sisson, W. Sullivan, and R. Karess. 2004. Reassessing the role and dynamics of nonmuscle myosin II during furrow formation in early Drosophila embryos. *Mol. Biol. Cell.* 15:838–850. https://doi.org/10.1091/mbc.e03-06-0440

Shulman, J.M., R. Benton, and D. St Johnston. 2000. The Drosophila homolog of C. elegans PAR-1 organizes the oocyte cytoskeleton and directs oskar mRNA localization to the posterior pole. *Cell.* 101:377–388. https://doi.org/10.1016/S0092-8674(00)80848-X

Skau, C.T., and C.M. Waterman. 2015. Specification of Architecture and Function of Actin Structures by Actin Nucleation Factors. *Annu. Rev. Biophys.* 44:285–310. https://doi.org/10.1146/annurev-biophys-060414-034308

St Johnston, D., and J. Ahringer. 2010. Cell polarity in eggs and epithelia: parallels and diversity. *Cell.* 141:757–774. https://doi.org/10.1016/j.cell.2010.05.011

Stevenson, V.A., J. Kramer, J. Kuhn, and W.E. Theurkauf. 2001. Centrosomes and the Scrambled protein coordinate microtubule-independent actin reorganization. *Nat. Cell Biol.* 3:68–75. https://doi.org/10.1038/35050579

Stevenson, V., A. Hudson, L. Cooley, and W.E. Theurkauf. 2002. Arp2/3-dependent pseudocleavage [correction of psuedocleavage] furrow assembly in syncytial Drosophila embryos. *Curr. Biol.* 12:705–711. https://doi.org/10.1016/S0960-9822(02)00807-2

Takatsuki, H., E. Bengtsson, and A. Månsson. 2014. Persistence length of fascin-cross-linked actin filament bundles in solution and the in vitro motility assay. *Biochim. Biophys. Acta.* 1840:1933–1942. https://doi.org/10.1016/j.bbagen.2014.01.012

Tepass, U. 2012. The apical polarity protein network in Drosophila epithelial cells: regulation of polarity, junctions, morphogenesis, cell growth, and survival. *Annu. Rev. Cell Dev. Biol.* 28:655–685. https://doi.org/10.1146/annurev-cellbio-092910-154033

Turner, F.R., and A.P. Mahowald. 1976. Scanning electron microscopy of Drosophila embryogenesis. 1. The structure of the egg envelopes and the formation of the cellular blastoderm. *Dev. Biol.* 50:95–108. https://doi.org/10.1016/0012-1606(76)90070-1

Vaccari, T., C. Rabouille, and A. Ephrussi. 2005. The Drosophila PAR-1 spacer domain is required for lateral membrane association and for polarization of follicular epithelial cells. *Curr. Biol.* 15:255–261. https://doi.org/10.1016/j.cub.2005.01.033

Webb, R.L., M.N. Zhou, and B.M. McCartney. 2009. A novel role for an APC2-Diaphanous complex in regulating actin organization in Drosophila. *Development.* 136:1283–1293. https://doi.org/10.1242/dev.026963

Wu, Y., and E.E. Griffin. 2017. Regulation of Cell Polarity by PAR-1/MARK Kinase. *Curr. Top. Dev. Biol.* 123:365–397. https://doi.org/10.1016/bs.ctdb.2016.11.001

Xia, S., Y.B. Lim, Z. Zhang, Y. Wang, S. Zhang, C.T. Lim, E.K.F. Yim, and P. Kanchanawong. 2019. Nanoscale Architecture of the Cortical Actin Cytoskeleton in Embryonic Stem Cells. *Cell Reports.* 28:1251–1267.e7. https://doi.org/10.1016/j.celrep.2019.06.089

Zallen, J.A., Y. Cohen, A.M. Hudson, L. Cooley, E. Wieschaus, and E.D. Schejter. 2002. SCAR is a primary regulator of Arp2/3-dependent morphological events in Drosophila. *J. Cell Biol.* 156:689–701. https://doi.org/10.1083/jcb.200109057

Zhang, Y., H. Guo, H. Kwan, J.W. Wang, J. Kosek, and B. Lu. 2007. PAR-1 kinase phosphorylates Dlg and regulates its postsynaptic targeting at the Drosophila neuromuscular junction. *Neuron.* 53:201–215. https://doi.org/10.1016/j.neuron.2006.12.016

Zhang, Y., J.C. Yu, T. Jiang, R. Fernandez-Gonzalez, and T.J.C. Harris. 2018. Collision of Expanding Actin Caps with Actomyosin Borders for Cortical Bending and Mitotic Rounding in a Syncytium. *Dev. Cell.* 45:551–564.e4. https://doi.org/10.1016/j.devcel.2018.04.024

Zuo, Y., W. Oh, and J.A. Frost. 2014. Controlling the switches: Rho GTPase regulation during animal cell mitosis. *Cell. Signal.* 26:2998–3006. https://doi.org/10.1016/j.cellsig.2014.09.022